Iron-oxide based electrodes in aqueous supercapacitors

A Thesis

Submitted to the Faculty

of

Drexel University

by

Rahul Nagesh Neeta Pai

in partial fulfillment of the

requirements for the degree

of

Masters of Science in Chemical Engineering

June 2017

Dedications

I dedicate this thesis to my supportive and loving family. To my parents Nagesh Ramdas Pai and Neeta Nagesh Pai; to my brother Prashant Nagesh Pai; to the memory of my grandparents Ramdas Pai and Uma Ramdas Pai.

Acknowledgements

This work would not have been possible without the guidance and assistance of my professors, colleagues, and the support of my family and friends. Firstly, I would like to express my gratitude for my advisor, Prof. Vibha Kalra, for accepting me in her research group, her constant motivation, support and guidance throughout my master's program. I admire her mentorship, work ethics, intelligence and critical reasoning skills. I would also like to thank all the members of my thesis committee, Prof. Kenneth Lau and Prof. Maureen Tang for their valuable time, comments and suggestions on my thesis. I am very thankful to Prof. Joshua Snyder for allowing me to use the equipment in his lab.

I would also like to acknowledge Dr. Dmitri Barbash for training and helping me with X-Ray Diffraction (XRD) technique, Dr. Mykola for Brunauer, Emmett and Teller (BET) measurements and Andrew Dillon for conductivity measurements, which helped me in characterizing my materials for my research work. I would also like to thank Swarnendu Chatterjee for his help to use Radio- Frequency furnace, centrifuge and providing me with de-ionised water.

I am extremely grateful and blessed to have a such an amazing group of people at Kalra research group, Ali , Ayda Rafie, Dr. Arvinder Singh, Caitlin Dillard, Daniel Lawrence, Dr. Richa Singhal and Dr. Silas Simotwo for their help, critical reasoning to my thoughts, guidance and helpful discussions throughout my research period.

I would also like to thank chemical and biological engineering department staff, Andrea Falcone for being so nice and helping me with all the administrative and academic problems

Table of Contents

LIST OF TABLES

LIST OF FIGURES

Abstract

Redox materials based carbon nanofibers for energy storage devices.

Rahul N. Pai

Advisor: Dr. Vibha Kalra

Climate change and the limited availability of fossil fuels have greatly affected the world economy and ecology. The demand of energy is not coping up the supply of the same. With a fast-growing market for portable electronic devices and the development of hybrid electric vehicles, there has been an ever increasing and urgent demand for environmentally friendly high-power energy resources. This has led to development of energy storage devices, mostly supercapacitors and batteries. In the recent times it is seen that li-ion batteries have been dominating energy storage device sector (Portable electronics, hybrid vehicles and grids). Li-ion still lacks when there is sudden demand in high power. The development of higher energy and power density systems highly rely upon the advancement of new materials used in these devices. Transition oxides and conducting polymers based nanofibers are excellent candidates for application as electrodes in the energy storage devices because of their unique properties such as high capacitance, chemical durability, nature friendly and high specific surface area.[1] Electrospinning is a simple, fast and a scalable technique wherein fiber formation is done with the help of a strong electric field to stretch out a polymer solution to form nanofibers with diameters in the range of 100–800 nm. This fiber-formation technique results in formation of free-standing, binder free and non-woven fiber mat. My thesis focuses on preparation of Iron oxide based nanofibers through electrospinning method,

characterizing these nanofibers via spectroscopic/microscopic techniques and developing understanding of their electrochemical mechanisms in an aqueous medium. My work focusses more on structurally supporting these oxides in the conductive carbon fiber matrix which otherwise delaminates while cycling reducing performance in energy storage devices.

Chapter 1. Introduction

Climate change and the limited availability of fossil fuels have greatly affected the world economy and ecology. The demand of energy is not coping up the supply of the same. With a fast-growing market for portable electronic devices and the development of hybrid electric vehicles, there has been an ever increasing and urgent demand for environmentally friendly high-power energy resources. This has led to development of energy storage devices, mostly supercapacitors and batteries[2]. In the recent times it is seen that li-ion batteries have been dominating energy storage device sector (Portable electronics, hybrid vehicles and grids). Li-ion still lacks when there is sudden demand in high power. This is associated to its low power density. Power density of energy storage systems plays an important role in starting up diesel locomotives and accelerating a hybrid vehicle. For such applications supercapacitors are under consideration. Hence they have attracted growing attention owing to their high power density and safety performance. In addition, the slow faradaic behavior in li-ion batteries to stores energy, wherein the lithium ions move from one electrode to the other during charging and discharging can be completely ignored in supercapacitors, as they rely on absorption and desoroption of electrolyte ions on the porous electrode surface due to electrostatic force. Thus, compared to the rate of ions inserting into and extracting from electrodes, supercapacitors are able to charge and discharge much faster by absorbing and desorbing charges on the surface of electrodes which increases power density of supercapacitor. The above advantages of supercapacitors have made them promising

candidates to serve as the next generation energy storage technology. Advancement in development of new novel materials for high utilization and energy storage is always in progress. Most of these newly developed lab scale materials synthesized are powder based materials which are further blended with polymers such as PTFE (Polytetrafluoroethylene) and PVDF (Polyvinylidene fluoride) which act as binders. These binders act as insulators and hinder the performance of the electrodes by adding dead weight and decreasing the porosity of porous materials. Simultaneously, using these powdered active materials and conductive carbon, slurry is formed which is drop casted on substrates. Which create problems for scale-up as these substrates add up to the dead weight of these electrochemical devices. Thus development of new materials should primarily focus on having binder free and free standing electrodes.

Electrode material with desirable properties is the key for realizing high performance supercapacitors. In the thesis work, conducting polymers, transition-metal-oxide-based nanostructures, as well as composite materials consisting of transition metal oxide and carbon nanofibers (CNFs) were prepared, characterized and evaluated as supercapacitor electrodes. CNFs are promising candidates for application as electrodes in energy storage system (ESS) owing of their unique properties such as high mechanical strength, high electrical and thermal conductivities, high chemical stability, flexibility, and high specific surface area. CNFs were fabricated using a simple yet versatile technique of electrospinning. This technique uses a strong electric field (DC-Kilo Volts) to pull or thin out a polymer solution or melt jet forming ultrathin fibers with diameters in the range of 50–500 nm. This continuous fiber-formation technique inherently forms a free-standing non-woven fiber mat, thus, potentially allowing their direct application without addition of

any binders. The fibers can be intentionally made non-woven or aligned based on stationary or rotating drum collector respectively.

CNFs and their composites which have been fabricated in this work are free-standing with a continuous interconnected 3-D network providing fast ion-diffusion as well as fast transport of electrons within the network, a good electrode and electrolyte contact, a characteristic essential for efficient energy storage, also allowing it to be directly used in any ESS without any further processing.

CNFs with controlled pore architectures and enhanced functionalities were fabricated and characterized as cost-effective and performance-effective electrodes for supercapacitors. Studies were conducted and focused to understand their electrochemical behavior as well as reaction mechanism. Chapter 1 provides the introduction to electrochemical energy storage systems, their working operation and challenges associated with them, motivation of using carbon nanofibers as electrodes in these systems. Chapter 2 discusses techniques towards characterizing pseudocapacitive materials for energy storage systems. Chapter 3 discusses about a facile route to fabricate free standing, binder free Iron-oxide based carbon nanofibers. Chapter 4 comprises of primitive usage of cobalt oxide nanoparticles for application of asymmetric supercapacitor electrodes in aqueous region.

1.1. Electrochemical Energy systems

Electrochemical energy storage is used in wide variety of fields ranging from portable electronics to hybrid electric vehicles. To satisfy the requirements for these energy storage devices, the application particular devices needs to have advantages in terms of both the amount of energy stored and the maximum power. Weight, initial cost, and lifetime are also important issues. The ever-increasing energy needs, rapid depletion of fossil fuels, and environmental concerns has directed the research efforts towards developing alternative energy resources that are both sustainable and renewable. However, renewable energy sources like sun and wind have disadvantages that they are not available all the time and throughout the year. Moreover, the transformation to electric vehicles is of utmost importance to reduce the dependence on oil and reduce the CO_2 emissions. The main obstacles for electric vehicles are performance and cost of the battery systems. The performance of the battery systems is quantified by usable energy density, power density, and cycle lifetime. The two critical parameters characterizing the EES systems are energy density and power density while energy density characterizes the amount of energy stored, power density is the measure of how quickly the stored energy can be delivered Future demanding energy applications require a blend of high energy density and high power density materials. The traditional capacitor is charged from primary energy storage units. Traditional capacitors are very low energy density materials. They are unable to provide high power and energy where significant energy is

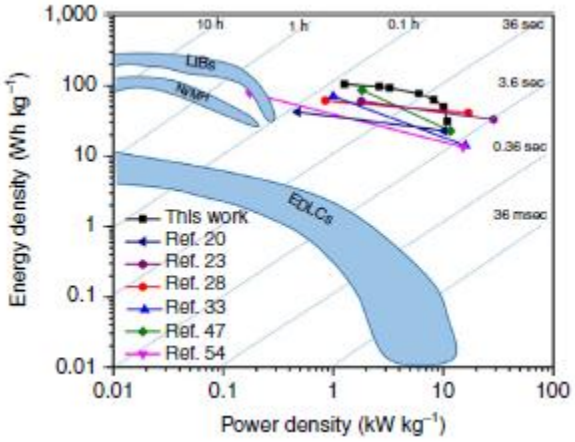

Figure 1.1 Ragone Plot of various energy storage devices

needed. Therefore, the development of high energy density capacitors (supercapacitors or electrochemical capacitors) has been undertaken by various groups all over the world. In Fig.1.1, Ragone plot, further explains us various energy storage devices and their power density and energy densities which can be used to explain their roles in different energy storage devices. Among all the energy storage devices, batteries have become the most common ones and are involved in most applications, because they can store large amounts of energy in a relatively small volume and weight, which is suitable for many applications. However, the disadvantages lie in the shelf and cycle life with most types of batteries. Supercapacitors on the other side lie on the left hand side if the Ragone plot and we can see that they deliver high power density but less energy density. Advantages of supercapacitor lie in high power density and longer shelf and cycle life than batteries. The objective of current energy storage devices is to move towards the upper right-hand corner of this plot. Thus, development of electrochemical energy storage (EES) systems, such as advanced rechargeable batteries and electrochemical capacitors, to meet the higher requirements of future systems is essential. The

development of higher energy density and power density EES systems, in turn, significantly depends on the advancement of new materials used in these devices

1.2. Introduction of Supercapacitors

In 1957, the first supercapacitor was developed by General Electric *[Becker]*. Applying a double-layer mechanism, it was considered that this supercapacitor stored energy in the carbon pores and showed exceptionally high capacitance. In 1966, the Standard Oil Company, Cleveland (SOHIO) invented the first supercapacitor device which stored energy at a double-layer interface. From then on, the development of supercapacitors proceeded very quickly, and they are of particular interest in automotive applications for hybrid vehicles and as supplementary energy storage for battery electric devices.

Electrochemical capacitors (also known as supercapacitors, or ultra-capacitors) are one of the important EES systems because of their high power density and long cycle life. They have a higher power delivery or uptake of ~10 Wh kg-1, however, much lower energy density (~5 Wh kg-1) than batteries. Supercapacitors are classified into electric double layer capacitors and pseudocapacitors, based on the energy storage mechanism (Mechanisms explained further). Electric double layer capacitors (or, EDLCs) store energy electrostatically using reversible adsorption of ions (of the electrolyte) at the electrode-electrolyte interface under an applied potential. This process allows capacitors to deliver energy rapidly, thereby providing high power density, but only in small amounts (thus, have low energy density).

The materials based on double-layer charge storage mechanism have limited specific capacitance, typically in the range of 10-50 μF cm-2. In this respect, pseudocapacitors

are being considered and developed. Pseudocapacitors utilize fast and reversible redox reactions at the electrode-electrolyte interface to store charge.

Pseudocapacitors can provide 10-100 times greater capacitance than EDLCs, making them highly desirable for next generation supercapacitors. The most studied pseudo capacitive materials include metal oxides (e.g. RuO2, MnO2, etc.) and conducting polymers (e.g. polyaniline, polypyrrole, etc.), which are either expensive, operate in low voltage windows, toxic or have low cycling stability. The major challenges facing the development of supercapacitors include low energy density and and a lower operating window. Thus, fabrication of materials with pseudocapacitive properties as well as low-cost, high capacitance and operating in a significantly wide windowl is desired.

The growing crisis of fossil fuels and the severe environmental pollution resulting from exhaust gas of internal combustion engine have made researchers focus on developing new energy storage devices to replace conventional engines. Great effort has already been made towards developing hybrid powers, fuel cells, and chemical cells. However, due to their short service life, high cost and low temperature performance, it is hard to solve all the problems at the same time. The emergence of supercapacitors which have outstanding features such as long cycling life, high temperature performance and environmental benignity, has opened a way to solve almost all the problems that are faced by current energy storage technologies. Because of the advantages of supercapacitors, they can replace conventional batteries or even novel energy storage devices utilized in electrical vehicles. Moreover, supercapacitors have more widespread applications than traditional batteries. Therefore, many researchers are sparing no efforts to study the electrode materials of supercapacitors.

1.2.1. Electrolytic capacitor

The discovery of electrolytic capacitors was a coincidence when researchers were conducting experiments for fuel cells and secondary batteries using porous carbon as the electrode in early 1950s. Researchers found that porous activated carbon (AC) with high specific surface area could be used for energy storage. Although the mechanism of electric double layer had not been thoroughly studied, the first “Low voltage electrolytic capacitor with porous carbon electrode” was still reported in 1957 by H.I. Becker.

Electrolytic capacitors are energy storage devices with a metal as anode, metal oxide layer on the surface of anode as the dielectric and the electrolyte as cathode. The various electrolytic capacitors available in the market are as follows aluminum electrolytic capacitors, tantalum electrolytic capacitors and niobium electrolytic capacitors. However the capacitance of electrolytic capacitor is less and researchers were not able to improve the performance of these electrochemical capacitors.

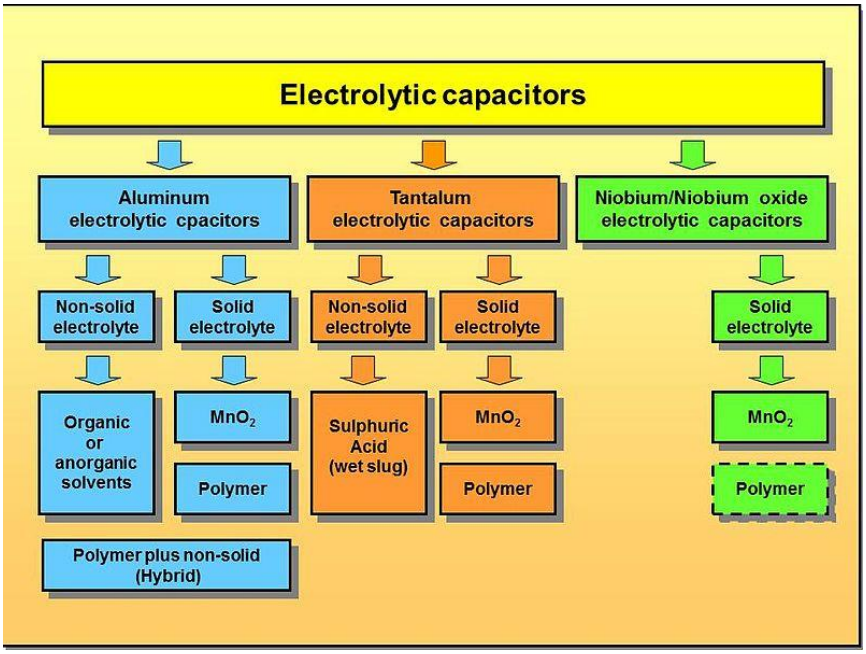

Figure 1.2 Various electrolytic capacitors

1.2.2. Supercapacitors

In the early stage, electrodes of electrochemical capacitors were usually made of activated carbon coating on metal foil and the electrodes were soaked in liquid or solid electrolyte with a porous separator between them. This design was the basis of the electrochemical capacitors, which greatly increased the capacitance to the order of 1 farad. In 1971, this invention was commercialized as “supercapacitors” (SCs) by a Japanese company, NEC Corporation. At that time, SCs only had limited applications and were used as back-up power supplies [7]. The capacitance of the primitive SCs was mainly in a weak position because of the large internal equivalent series resistance (ESR), resulting from the low conductivity of electrodes and electrolytes. These problems were basically solved with advancements in the electrode materials and the electrolyte; when large amount of SCs were marketed, most of them were applied in the military due to their high cost. In early 1975 to 1980, Brain Evan Conway (B.E Conway), a researcher

form the University of Ottawa, conducted a large number of experiments using ruthenium oxide (RuO_2) as an electrode material. This rare earth metal oxide had significant properties which helped in storing charges electrostatically by electrical double layer and also by pseudocapacitance which resulted from fast surface faradaic reactions. His research guided and extended future work on supercapacitors and he explained the difference between batteries and supercapacitors in his book, “electrochemical supercapacitors”[2]

1.2.3. Hybrid Supercapacitors

Recently, in order to combine the high power density of SCs and the high energy density of the batteries, hybrid capacitors have been popular in the research which are also known as hybrid asymmetric supercapacitors. This technology was first reported by FDK Company who used carbon and pre-doped lithium-ion as the electrode materials in 2007. As can be seen in from the ragone plot, hybrid asymmetric capacitors have at least one magnitude higher energy density than electrode double layer capacitors (EDLC). However, the power density of hybrid asymmetric capacitors are comparable with EDLCs. Most of them employ organic electrolytes and they possess risk to health at times of leakage. Compared with dangerous organic electrolytes, aqueous supercapacitors hold more promise. Meanwhile, novel electrode materials are highly demanded for aqueous supercapacitors to increase the capacitance, overpotential against water splitting reactions and improved stability.

1.3. Design of Supercapacitors

A typical structure of a supercapacitor involves two electrodes, anode (-ve) and cathode (+ve), soaked in electrolyte connected to the current collectors with a separator (insulating material) in between them. Potential is applied between the electrodes to polarize and charge the device. The insulating separator located between two electrodes is ion-permeable but can prevent electrons from passing through, hence preventing short circuit. Both electrodes and the separator is immersed into electrolyte, which contains positive and negative ions. Under the influence of the applied potential, the ions with opposite polarity to the electrode will be absorbed onto the corresponding electrode, forming an electric double layer on the interface between the electrode and the electrolyte. The electric double layer model was firstly proposed by Helmholtz in 1853[2]. Helmholtz model can be simply described as a capacitor since he supposed that only a single layer of ions is absorbed on the surface. The electric double layer capacitance calculated by this model is shown in equation (1):

$$C = \varepsilon / d \tag{1}$$

where ε is the electrolyte dielectric constant, which is also known as permittivity of the electrolyte, and d is the thickness of electric double layer. Although, the Helmholtz model is not accurate enough to show the relation between capacitance and voltage, because Helmholtz failed to consider the resistance in the electrolyte which can lead to a different distribution of charges.

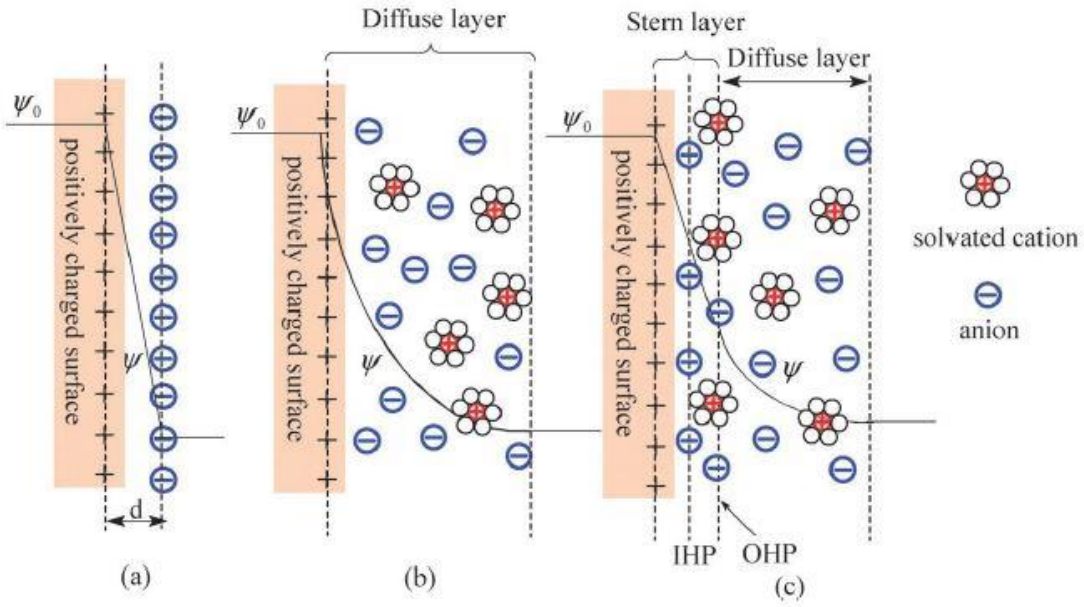

Figure 1.3 The relation of potential with distance away from interfacial layer between electrode and electrolyte in three models: Helmholtz's model (A), Gouy and Chapman's model (B), and Stern's model. Reproduced with permission from Zheng et al.

The Helmholtz model was later modified by Gouy and Chapman who proposed the existence of a diffuse layer of ions which leads to an exponentially decrease of the electric potential from the electrode surface to the bulk of electrolyte. As Gouy and Chapman did not involve the dimension of ions and molecules in their model, the relationship between surface capacitance versus surface potential cannot be described correctly especially at high surface potential. To solve this problem, Sterrn established a new model by combining theories of Helmholtz and Gouy and Chapman, which separates the space of

charges into two parts: the compact, formed by absorption of electrolyte ions and diffused layer, explained by Gouy and Chapman.[14, 15] Thus, the total specific capacitance C depends on the surface capacitance of the compact layermCc and the diffused layer Cd:

$$\frac{1}{C} = \frac{1}{Cc} + \frac{1}{Cd} \quad (2)$$

For a conventional capacitors or parallel electrode capacitors, their capacitance can be determined by the following equation:

$$C = \varepsilon r \varepsilon 0 A/d \quad (3)$$

where εr is the dielectric constant, $\varepsilon 0$ is the dielectric constant of vacuum, d is the distance between separated charges, and A is the surface area of the electrode. According to the electric double layer theory, large contact surface area of the electrode with electrolyte can increase the capacitance. Therefore, porous materials (e.g. activated carbon), which have large specific surface area (SSA) and are highly conductive, are ideal supercapacitors electrode materials and follow EDLC behavior. It is possible to imagine that each pore in the porous electrode works as a parallel capacitor. Thus, a supercapacitor is consists of billions of small electric double layer capacitors. When a supercapacitor is converted to a circuit model, it is necessary to involve the resistance of each pore, the external resistance and the membrane resistance.

1.4. Charge storage mechanisms of Supercapacitors

In traditional capacitors energy is stored on the two metal electrodes separated by a dielectric media, whereas in Supercapacitors energy storage is based on two separate mechanisms. Depending on whether a charge adsorption or faradaic reaction occurs in an energy storage process, the mechanism of charge storage of a supercapacitor is classified into electric double layer capacitance and pseudocapacitance. The capacitor which has electric double layer capacitance is called electric double layer capacitor (EDLC) because it stores energy in an electrostatic way by separating anions and cations in the electric double layer. The supercapacitor in which surface faradaic reaction takes place is called pseudocapacitor since it stores energy in an electrochemical way by having fast faradaic redox reaction on the surface of electrodes.

1.4.1. Electric Double Layer Capacitors

In an electric double layer capacitor, there is no faradaic reaction involved in the energy storage process leading to the major difference from batteries whose electrodes have redox reaction during charging and discharging processes. On the electrodes of electric double layer capacitor, there are only absorption and desorption of ions when external voltage is applied due to electrostatic charge separation. Thus, the electrode polarization of electric double layer capacitor is much faster than batteries due to the absence of limitation of chemical reaction kinetics occurring through reactions. The fast charge and discharge features of supercapacitors can lead to better power density than that of batteries. From the Ragone Plot shown in Figure 1.1, double layer capacitors have one magnitude higher power density than LIBs, solar batteries and fuel cells. In addition, faradaic reactions that occur in active materials on the electrodes may result in the swell or dissolve of active materials during charge and discharge. For example, the dendritic Li

growth on the electrode during charge and discharge may penetrate the separator between two electrodes and causes a short circuit or even explosion. Lithium sulfur batteries also suffer from the loss of active electrode materials because sulfur can convert to dissolvable products during charge and discharge, which is well known as the “shuttle effect”. However, electric double layer capacitors take the advantage of absence of faradaic reaction, so generally, double layer capacitors can maintain over 100,000 cycles. Compared with SCs, batteries can only survive thousands of cycles. Besides, double layer capacitors have more choices in terms of the electrolyte. Unlike batteries, the reactions of electrodes and electrolytes are fixed at certain potentials, double layer capacitors can adopt various electrolytes as their charge storage is based on adsorption.

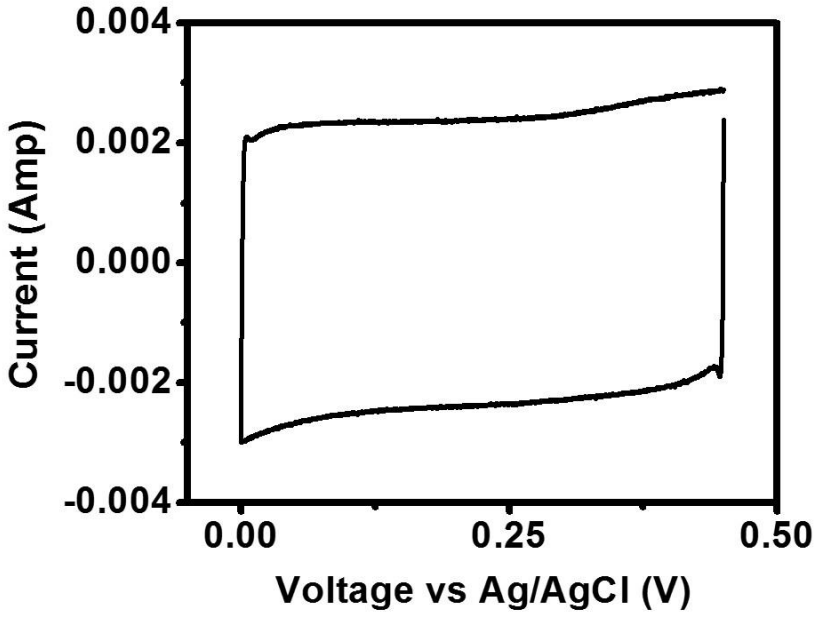

Figure 1.4 Activated carbon (EDLC)-Cyclic voltammogram

1.4.2. Pseudocapacitors

Electrochemical capacitors are designed by using the active materials which can have fast and reversible reaction on the surface of electrodes. Due to the presence of faradaic reactions, electrochemical capacitors are similar to batteries. Thus, electrochemical capacitors are also called pseudo-capacitors, and the capacitance of electrochemical capacitors is defined as pseudocapacitance. When a voltage is applied on the two electrodes of electrochemical capacitors, faradaic redox reaction occurs on the surface of the electrode to transfer charges between electrodes and the electrolyte, generating circuit in the electrochemical capacitors system. Transition metal oxides such as MnO_2, RuO_2, NiO, Co_3O_4, and V_2O_5 are common active materials of electrochemical capacitors[3-5]. In addition to conventional transition metal oxides, materials that possess pseudocapacitance also include: ternary metal oxides and metal hydroxides such as $NiCo_2O_4$, $ZnCo_2O_4$, $Ni(OH)_2$ and $Co(OH)_2$ metal sulfides; and conductive polymers such as polypyrrole, polyaniline, and polythiophene[4, 6-8].

Generally, pseudocapacitance is higher than electric double layer capacitance because electrochemical capacitors not only store electrical energy on electrode surface but also store energy in the bulk of the electrode near the surface. The average specific capacitance of AC is only 150 F/g whereas specific capacitance of some pseudo-capacitors can reach over 1000 F/g[9]. Therefore, electrochemical pseudocapacitors are able to provide higher energy density than electric double layer capacitance according to the Equation 4.

$$E = \frac{CV^2}{2} \quad (4)$$

where E refers to energy, C is the capacitance, and V is the potential window of the capacitor. Some electrochemical processes can even increase the working potential window to further enhance the energy density. However, the rate of electrochemical processes is limited by chemical kinetics, resulting in the sacrifice of the power density. Moreover, electrochemical capacitors also suffer from poor cycle life due to the presence of reversible redox reaction, which can lead to loss of active materials by either expansion and further dissolution or conversion to other non-faradaic material. In short Pseudocapacitors bridge the gap between conventional supercpacitors (EDLC) and Batteries (faradaic).

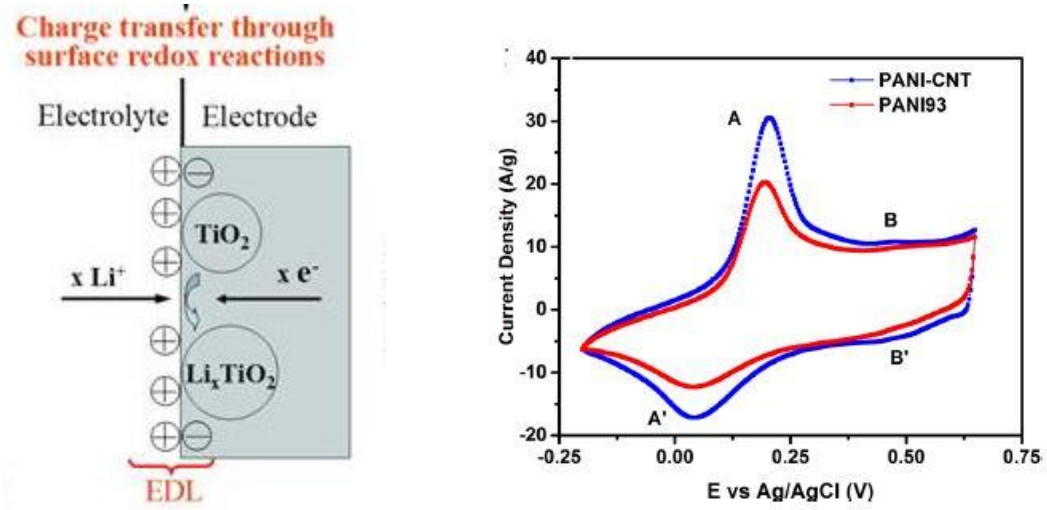

Figure 1.5 (a) Schematic of Pseudocapacitance (b) Polyaniline and Polyaniine CNT as a Pseudocapacitive electrode.

1.5. Energy density and Power density

In the structure of a supercapacitor, the two electrodes are able to be treated as two capacitors in series. Thus, the total capacitance of a supercapacitor can be described using the following equation:

$$CT = (C1 * C2)/(C1 + C2) \quad (5)$$

Herein, CT is the total capacitance and C1, C2 are individual capacitance of each electrode. When the materials of two electrodes are same, C1 is equal to C2. According to equation (5), the total capacitance is half of individual capacitance of one electrode. This type of SCs is called symmetric supercapacitors. On the other hand, if C1 is not equal to C2, which illustrates the materials of two electrodes are different, the corresponding supercapacitors are named asymmetric supercapacitors. Based on Equation (5), the total capacitance of asymmetric supercapacitors is mainly determined by the electrode which has lower capacitance. Depending on the total capacitance and the operational voltage of the supercapacitor, it is possible to evaluate the total energy that can be stored in this device. In addition, the power of a supercapacitor is given by the following equation:

$$P = \frac{V^2}{4Rs} \quad (6)$$

where Rs represents the equivalent series resistance (ESR) of a supercapacitor. ESR generally derives from the intrinsic resistance of electrode materials and electrolyte, transfer resistance of the diffusion of ions from electrolyte to the surface of the electrode as well as the resistance between electrodes and current collectors due to poor contact. Hence, in order to achieve a high power, it is necessary to reduce the inner resistance of a supercapacitor. On the other hand, since the value of power is proportional to the square of voltage, extending the potential window of a supercapacitor is a more effective way to increase the power. Basically, the potential window is associated with the intrinsic

property, structure of the electrode materials and the stability of the electrolyte. With regard to energy density, it can be determined by Equation (4). In addition to increasing the potential window, enhancing the specific capacitance of a supercapacitor is also beneficial for its energy density. The specific capacitance is defined as the amount of capacitance possessed by unit mass of a material. The relationship of specific capacitance and mass is indicated by the following equation:

$$Cs = \frac{CT}{W} \tag{7}$$

where Cs is the specific capacitance whose unit is F/g, CT is the total capacitance of an electrode whose unit is Faraday (F), and W is the weight of the electrode whose unit is gram (g). However, although some materials have extremely high theoretical specific capacitance, they may be unable to exert their capacitance completely in practical operation because of the low utility ratio of electrodes. On one hand, the utility ratio is hampered by the bad diffusion of electrolyte ions, which makes the ions fail to arrive at the whole surface of the electrode. On the other hand, poor conductivity of the electrode materials can also reduce the utility ratio of an electrode by impeding the formation of an electric double layer or by retarding the reversible redox reactions. Thus, to boost the utility ratio of an electrode, it is essential to build an electrode structure with effective electrons and ions transition channels (good interconnectivity and porosity).

1.6. Electrospinning and Binder Free Fabrication.

Electrospinning is a simple and a widely scalable process which helps in fabrication of woven or non-woven polymer mats which can further be pyrolysed in an inert environment to make free standing carbon nanofiber mats[10]. An electrospinning setup consists of three parts, metallic needle fixed to syringe with polymeric blend, a high voltage source and a metal collector. The solution is pumped at a fixed volumetric flow rate by a syringe pump. A high voltage is applied in the range of 1 to 30 Kilo Volt resulting in an even distribution of electric charge over the surface of the polymer drop at the needle tip. The drop then experiences electrostatic repulsion of the surface charges and a Coulombic force exerted by the electric field. The drop at the spinneret tip elongates as the intensity of the applied electric field is increased, which results in the formation of a conical surface known as a Taylor cone. When the force of the external electric field surpasses a threshold value, the surface tension of the polymer solution is overcome by the electrostatic forces and a charged liquid jet comprising the polymer solution is ejected from the Taylor cone tip. The solvent evaporates as the jet travels through the air, resulting in polymer fibers that are then collected on a grounded collector plate at a fixed distance from the needle tip. The

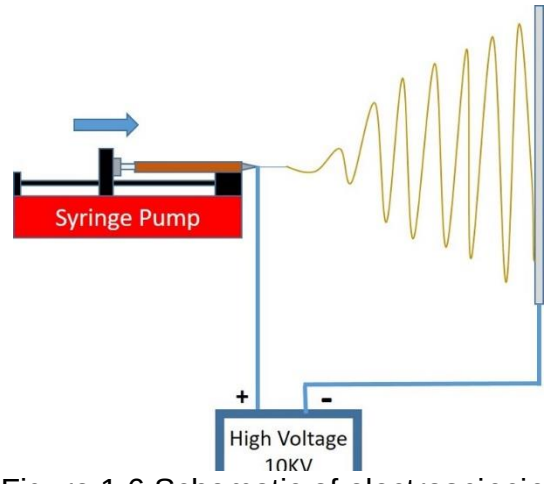

Figure 1.6 Schematic of electrospinning setup

fibers are typically deposited on the collector plate in a nonwoven manner – that is, the resulting polymer mat is composed of randomly oriented fibers. Figure 1.6: Schematic of a conventional electrospinning setup. Fibers can also be fabricated in a woven format by simple revolving the collector plate, to get fibers oriented in one single direction. Despite the simplicity of its setup, the electrospinning mechanism involved in this process is complex. It was initially thought that the formation of nanofibers was the result of the electrically charged jet splitting into several jets due to the repulsion among the surface charges. However, high-speed photography allowed researchers to disprove this theory. Photographs taken at high speeds of a jet undergoing electrospinning are presented in Figure 1.7. It is obvious from these images that the jet is initially a straight line and becomes unstable at some point during the electrospinning process. The single jet then undergoes a rapid whipping motion when it becomes unstable. The instability of the electrically charged jet, known primarily as bending or whipping instability, is attributed to the “electrostatic interactions between the external electric field and the surface charges on the jet.” Figure 1.7: High-speed photographs of a polymer jet undergoing electrospinning shows elongation of the polymeric solution. Another benefit of electrospinning, besides the simplicity of operating the technique, is that the morphology and diameter of the generated fibers is easily modulated by several parameters of the electrospinning process. The key parameters which have significant effect on the diameter of the fibers are the polymeric blend concentration, the flow rate of the solution and the potential applied between the collector plate and the needle. By tweaking any of the parameters one can get desired size of the fibers. The final morphology as a result of electrospinning is smooth interconnected fibers.

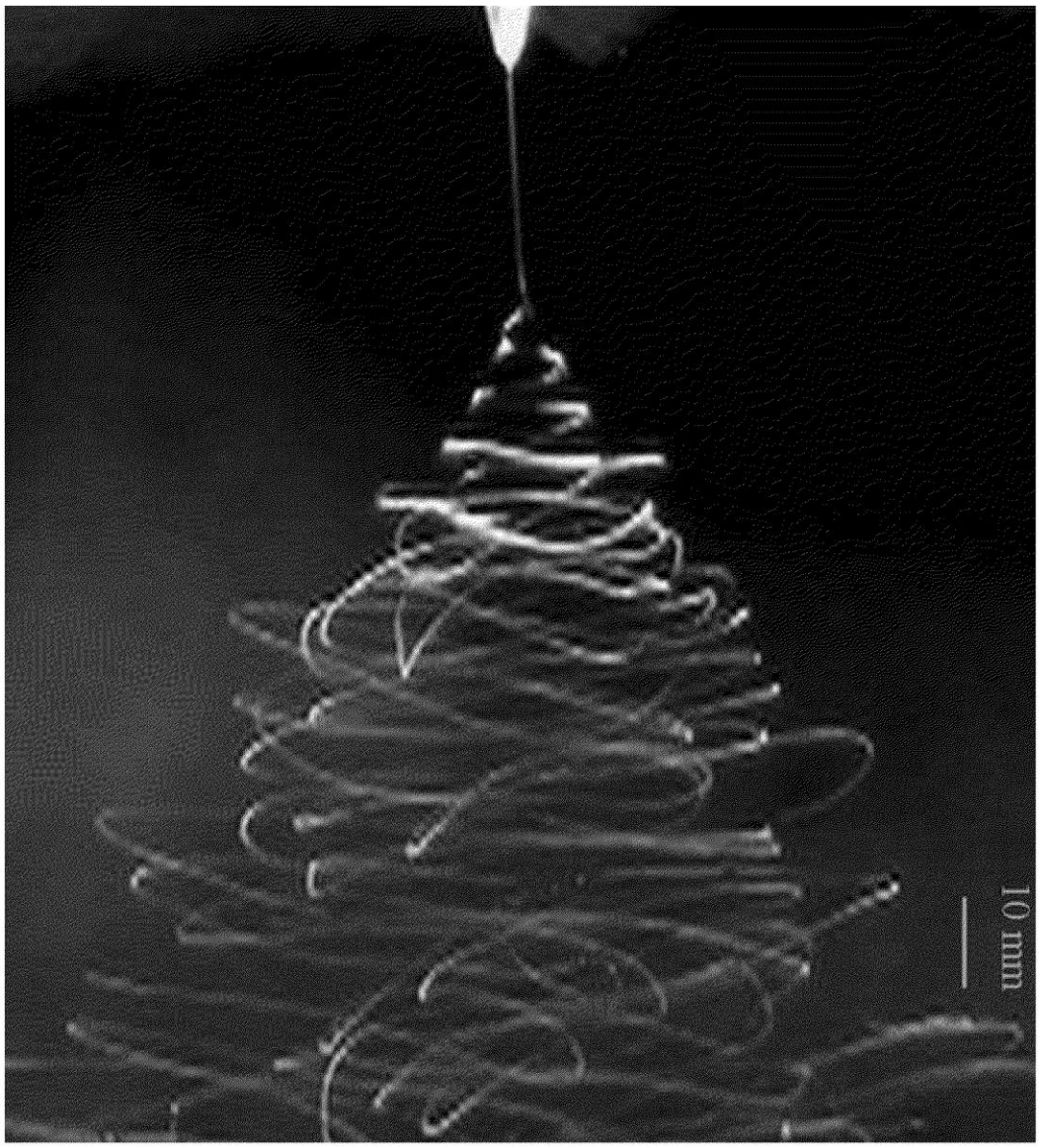

Figure 1.7 High defination photograph of electrospinning process

1.7. Materials for Supercapacitors

1.7.1. Electric Double Layer Capacitance

1.7.1.1 Carbon Materials

Carbon materials are found to be suitable materials for supercapacitors electrodes due to their abundance in nature, low cost, environmental friendly, easy scalable processing, tunable pore size, high specific surface area, high electrical conductivity, good chemical stability and stable performance in wide range of temperature. Carbon materials are basically utilized in electric double layer capacitors. As shown in Figure 1.8, the cyclic voltammetry of carbon materials are approximately rectangular without any redox peaks. With regard to the galvanostatic charge-discharge curves, the charge curves and corresponding discharge curves are basically symmetrical, indicating the high coulombic utility ratio of electrostatic energy storage method.

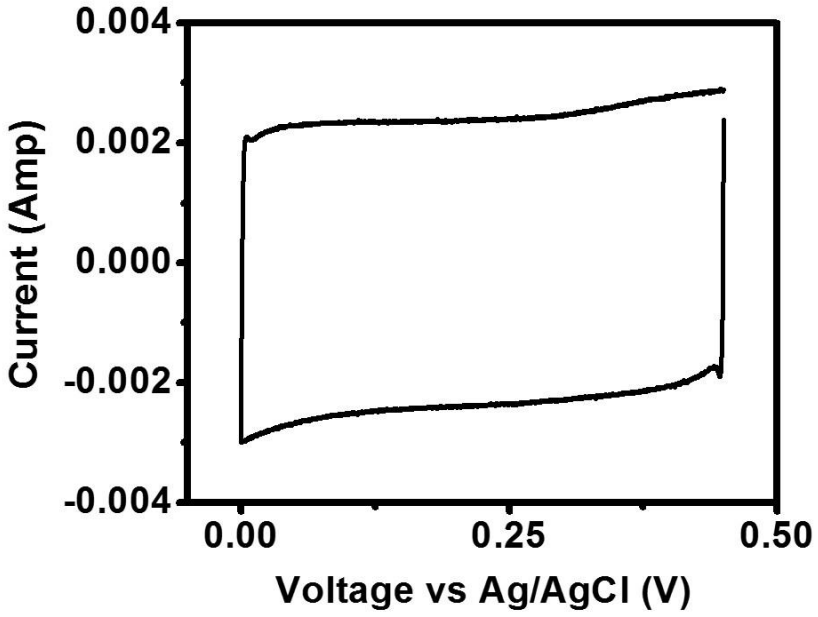

Figure 1.8 CV of AC

Since carbon materials are only able to store electrical energy on the surface of the electrode, the capacitance of carbon materials is mainly associated with the specific surface area, pore volume, pore size distribution, and conductivity. As reported in literature, among all the factors mentioned above, the performance of carbon materials are dominantly influenced by specific surface area and pore size distribution[11]. Currently many carbon materials with high surface area have been reported such as AC, templated porous carbon, carbon aerogels, carbon nanotubes (CNTs) and graphene. High specific surface area plays an essential role in supercapacitor electrode materials. Since carbonaceous materials only store energy on the interface between electrode and electrolyte by the absorption and desorption of charges, higher specific surface area can allow the electrode to accumulate more charges in unit mass materials. Based on Brunauer–Emmett–Teller (BET) theory, the specific surface areas (SSA) of different

carbonaceous materials are studied. SSA of commercial AC is between 500-1700 m^2/g. The surface area of activated carbon (AC) varies with the processing techniques. The highest surface area of AC can be more than 3000 m^2/g. surface area of templated porous carbons is mainly associated with the property of templates. Some templated porous carbons can achieve as high as 4000 m^2/g. In addition to specific surface area, pore size also has significantly effect on specific capacitance. In case of mesoporous carbon whose pore size is larger than 2 nm and smaller than 100 nm, the model showing the relation of pore size and specific capacitance with fixed surface area can be described in the following equation:

$$CA = \varepsilon r \varepsilon 0 b ln(bb - d) \quad (8)$$

where b is the radius of the pores, d is the distance between electrolyte ions and carbon surface. Recent study shows that when the pore size is below 1 nm, the capacitance increases sharply and reaches the maximum value when the pore size is the same as that of ions, indicating the highest capacitance is achieved when a single ion is in one pore[12].

1.7.1.1.1. Activated Carbon

Activated carbon materials not only have the general characteristics of carbonaceous materials such as having high conductivity, chemical stability, and application in a wide temperature range, but also have high surface area, making it preferred materials for supercapacitors. Activated carbon is enormously popular due to the low cost and facile processing techniques. Many carbonaceous materials, such as coke wood, and charcoal,

can be used as precursors of activated carbon. Materials with low degree of porosity are able to be processed to activated carbon by suitable activation including chemical activation, physical activation, and hybrid activation. Carbonization is usually applied to synthesize activated carbon, since most of other elements such as hydrogen, oxygen, and nitrogen are removed by the heat treatment in the inert atmosphere. After calcination, the carbonized materials only generate a little porosity. In order to largely increase the surface area of carbonized product, further activation using chemical treatment is necessary. To increase the efficiency of surface area, it is necessary to adjust the pore shape and size distribution of the porous structure.

1.7.1.1.2. Carbon Nanotubes

Carbon nanotubes are advanced carbon materials due to their superior properties such as high conductivity, good mechanical property, chemical and thermal stability, as well as the unique porosity. Based on directions of rolling a graphene sheet, carbon nanotubes are categorized as Zig-zag CNTs, chiral CNTs, and armchair CNTs. The atomic structures of various CNTs are shown in the following figure1.9[13]:

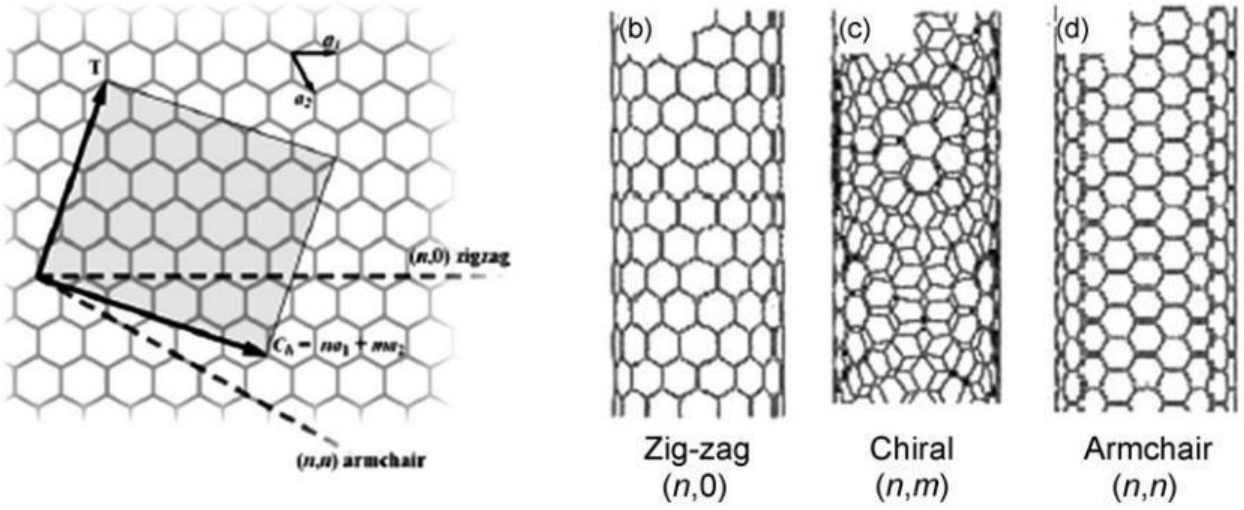

Figure 1.9 (a) Different atomic structures corresponding to the directions of rolling a graphene sheet. Atomic structure of Zig-zag CNTs (b), atomic structure of Chiral CNTs (c), and atomic structure of Armchair CNTs (d). Reproduced with permission.

CNTs are preferred for electrode materials for high power density devices owing to their low resistance. As mentioned above that the power is determined by Equation (6) which shows that a low resistance value can lead to high power density. Besides, the small resistance in CNTs is also able to show good rate capability. In addition to the good conductivity, the unique structure and mechanical stability has made CNTs good substrates for other active materials as well as perfect candidates for supercapacitor applications.

1.7.1.1.3. Graphene

Graphene is a two-dimensional carbon sheet formed by sp^2-hybridized. This specific structure is possible to be built into many other allotropes of carbon such as CNTs, graphite, and various other forms of carbonaceous materials. Graphene was discovered during the study of graphite when people tried to utilize fewer layers. A single layer graphene is composed of hexagonal sp^2 carbon atoms. The specific structure exhibits high mechanical stability, thermal stability, and great electrical property. In addition, graphene also has extraordinary high specific surface area which is required for superior performance of electric double layer capacitors. If the large specific surface area can be fully utilized, the specific capacitance of an EDLC is able to reach 600 F/g, proving that graphene is a promising materials for supercapacitor electrodes. Many graphene-based electrode materials of supercapacitors have been studied both in aqueous and organic electrolytes. Among the synthesis of these electrode materials, different methods have

been adopted such as chemical modification, microwave irradiation, thermal treatment of graphene oxide at high temperature, and at low temperature but in vacuum circumstance. Normally, the capacitance of aqueous supercapacitors with graphene electrodes is between 130 F/g and 200 F/g. The reason that the specific capacitance of practical graphene-based supercapacitors cannot reach theoretical specific capacitance of 550 F/g is mainly because that graphene sheet has high possibility of restacking during the preparation, leading to the lack of sufficient utilization of surface area in graphene.

Due to the high conductivity and mechanical stability, graphene is also suitable for using as the substrate for active materials like faradaic materials with pseudocapacitance. Although pure carbon materials are hard to achieve high energy density and power density for supercapacitors, they still play an important role in obtaining high-performance supercapacitors owing to their high surface area and superior conductivity. Currently, one strategy of developing supercapacitors with high power density and energy density is to uniformly coat a thin layer of faradaic materials on carbon materials

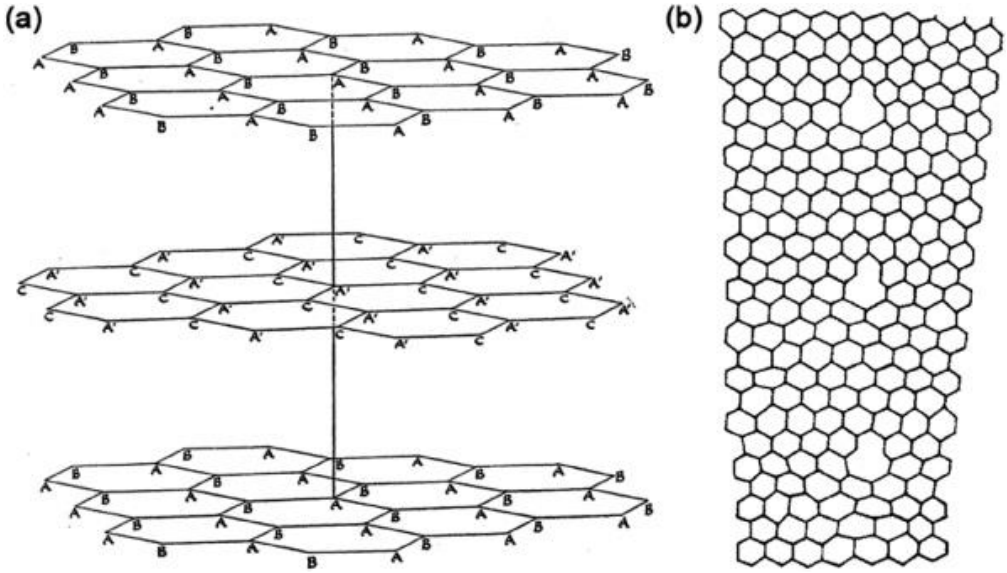

Figure 1.10 2D Graphene sheets

1.7.2. Faradaic Materials

Carbon materials store charges in the Helmholtz Double layer, faradaic materials store charges with fast redox reactions on the surface or in the bulk of the electrode near the surface. The specific capacitance of carbon-based materials is low. However, the specific pseudocapacitance is approximately 10-100 times higher than carbon materials, which is very promising for future energy storage devices. Therefore, pseudocapacitive materials are widely studied in recent years in order to develop advanced electrode materials for the next generation of supercapacitors. Typically, the pseudocapacitive materials are able to be divided into two categories: conductive polymers and transition metal oxides.

1.7.2.1 Conductive Polymers

Conductive polymers are generally low-cost, environmental friendly, and their source is extensive. Besides conductive polymers have high conductivity, wide potential widow, and high porosity, making them promising candidates for supercapacitor electrode materials. During charging and discharging process, redox reactions occur not only on the surface of the conductive materials but also in the bulk. When oxidation reaction occurs, ions are attracted from the electrolyte to the polymers, and released to the electrolyte during reduction. The redox reactions are highly reversible, since there is no phase transition, making conductive polymers competent for long cycle life. The conductive behavior of conductive polymers is mainly because conductive polymers are positively or negatively charged by oxidation or reduction processes. These specific oxidation and reduction processes are generally named as doping. Conductive polymers only have conductive property at a doped state. There are three types of conductive polymers commonly used as electrode materials for supercapacitors: polyaniline (PANI), polypyrrole (PPy), polythiophene (PTh), and their derivative materials. Since conductive

polymers are active and can work well only under certain conditions, it is important to use them in the right electrolyte and right potential ranges. For example, the negative doping potentials of PANI and PPy are usually lower than the reduction potential of electrolyte, therefore they can only be positively doped and better to be used as the cathode electrode materials. In addition, PANI performs better in acidic electrolyte, where contains the necessary protons for PANI during its charging and discharging[6]. The working potential window is also essential for conductive polymers. Under an improper potential, conductive polymers may be degraded or lose the conductivity. Thus, the potential range plays a key role in the performance of conductive polymer based supercapacitors.

1.7.2.2 Polyanilyne

Polyaniline (PANI) is a polymer whose conducting properties were traced back in 1952.It is a p-type conducting polymer which has attracted attention form researchers for its application in electrodes for energy devices either as a sole electrode active material or as a supplemental material to enhance performance. PANI is commonly synthesized through chemical oxidative polymerization of aniline using a strong oxidant. Electrochemical synthesis of polyaniline has also been widely applied. PANI can exist in three different oxidation states: leucoemaraldine, emaraldine base is the partially-oxidized and pernigraniline which are the fully reduced, partially oxidized and fully oxidized states, respectively. Synthesis of PANI is largely carried out in acidic conditions, which result in a doped emeraldine salt. External doping or de-doping of the emeraldine salt has also been achieved using an acid or base, respectively.[14] Conductivity of PANI is strongly dependent on the degree of oxidation and the doping. Doped emeraldine base is the most conductive state, with conductivity ranging from 0.1 to over 100 S/cm.[15] Un-

doped emaraldine and the fully reduced/oxidized states show conductivity in the order of 10^{-10} S/cm.

1.7.2.3 Transition Metal Oxides

Transition metal oxides (TMOs) are widely studied as the electrode materials for supercapacitors because of their variable oxidation states which contributes to higher capacitance. As faradaic materials, TMOs have two or more oxidation states in the same phases. When charging and discharging take place, TMOS are able to change their oxidation states and protons can insert into and extract from the oxide lattice during reduction and oxidation surface reactions. The redox reactions are fast and reversible, since no phase changing occurs in the process. Several TMOs such as RuO_2, MnO_2, V_2O_5, NiO, and Co_3O_4 have been found to have the above properties and been tested as supercapacitor electrode materials.

1.7.2.3.1. RuO2

Ruthenium oxide (RuO_2) has two prominent phases, viz. crystalline and amorphous hydrous phase, making it a promising electrode material that exhibits large electrochemical capacitance. The capacitance values exceeding 700 F g^{-1} are known to result from under-potential hydrogenation and oxygenation in acidic and alkaline electrolytes, respectively. RuO_2 has a high capacitance of about 150–260 F cm^{-2} which is about ten times higher than that of carbon. Such a high value is believed to be due to pseudocapacitance from the surface reaction between Ru ions and H ions. The *C*–*V* curve of RuO_2 in an H_2SO_4 electrolyte is mirror-like and mainly featureless within a potential range of 1.4 V. The advantages of amorphous ruthenium oxides include high *Sc*, high conductivity, and good electrochemical reversibility. The maximum *Sc* of

768 F g^{-1} has been obtained from an amorphous ruthenium oxide, which is at least two times greater than that from other capacitive electrode materials. In addition, the maximum potential range is about 1.35 V for amorphous ruthenium oxides and is greater than that measured for crystalline ruthenium oxides of about 1.05 V in aqueous electrolytes. The main disadvantage of RuO_2 is of it being toxic and costly[16].

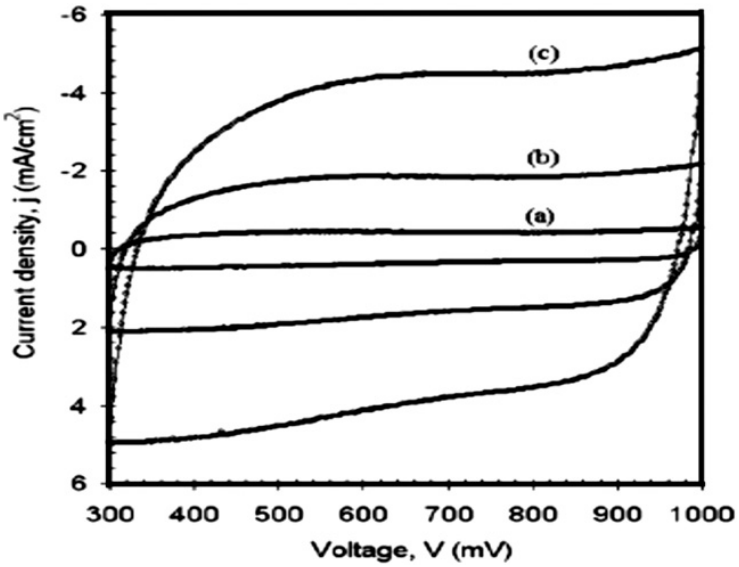

Figure 1.11 the typical cyclic voltammograms (CV) of sprayed ruthenium oxide electrode at various scan rates (10, 20, 50) mVs^{-1}[16].

1.7.2.3.2. MnO2

Manganese oxide (MnO_2) provides a lower cost and lower toxicity replacement for ruthenium oxide in supercapacitor applications. Composite electrodes based on MnO_2 and containing carbon nanotubes, carbon blacks, polyaniline and other conducting materials are under investigation for application in supercapacitors. Fig.1.12 shows typical cyclic voltammograms (CV) of chemically deposited MnO_2electrode at different scanning rates in 1.0 M Na2SO4 electrolyte. Here are several oxidation states, including Mn(0), Mn(II), Mn(III), Mn(IV), Mn(V), Mn(VI), and Mn(VII), for manganese oxides. The

reversibility of these redox transitions is usually too low to be applicable for the supercapacitors although MnO_2-based electrodes have been employed as the electroactive materials for batteries. The invariance of the manganese oxidation state for the composite electrode suggests that only a thin layer of MnO_2 is involved in the supercapacitive process. Direct evidence for the variance of the manganese valence for a crystallized form of MnO_2 was recently shown by in situ X-ray absorption near-edge structure. Water content in MnO_2 is known to affect the electrochemical reactivity and thermodynamic stability of various MnO_2 phases as it causes a variation in crystal lattice and a consequent variation in electrical conductivity and electrode potential. Two factors strongly influence the cycle life of the manganese dioxide film electrode: (i) manganese dissolution and (ii) the oxygen evolution reaction. Unfortunately, most of the MnO_2-based devices show about 20% reduced Sc after about 1000 charge/discharge cycles, highlighting the difficulty to achieve long-term cycling stability for a device[16].

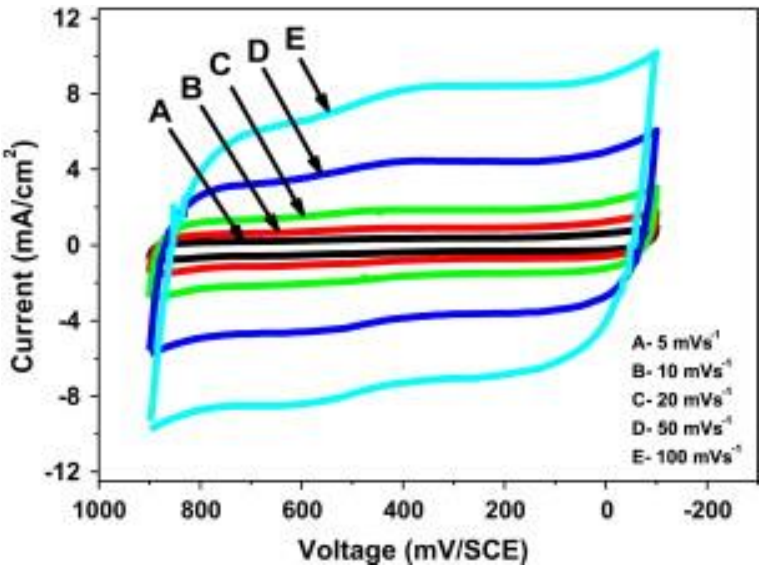

Figure 1.12 The typical cyclic voltammograms (CV) of MnO_2 electrode at different scanning rates; (A) 5, (B) 10, (C) 20 (D) 50 and (E) 100 mV s−1 in 1.0 M Na2SO4 electrolyte.

1.7.2.3.3. Cobalt oxide / Hydroxide

Co_3O_4 and CoOx are for promising materials for supercapacitors due to their intercalative pseudocapacitance properties. Lin et al. [103] obtained a maximum Sc of 291 F g−1 using CoOx xerogel calcined at 423 K. The cobalt oxide electrode has been found to have good efficiency and long-term performance and the good corrosion stability. The MWNTs/ Co_3O_4 composites show high capacitor property, and their best specific capacitance is up to 200.98 F g−1 which is significantly greater than that of pure MWNTs (90.1 F g−1)[16].

1.7.2.3.4. Nickel oxide (NiO) based supercapacitors

Nickel oxide based materials also have shown some degree of interest in supercapacitors. The defective nature of the nickel oxide could be utilized to improve its specific capacitance. The Sc was from 200 to 278 F g−1 in 1 M KOH within 0.5 V potential windows. Decreasing trend of supercapacitor value with electrode mass can be related to the starvation of active sites reacted with ions. Due to the slight phase change from nickel hydroxide to oxide through the intermediate stage of NiOOH, the redox peak was gradually reduced and caused collapse of its intrinsic lattice structure and showed diminution of its capacitance as follows equation

$$NiOOH + e \longrightarrow NiO + OH - \quad (9)$$

. The specific capacitances of the NiO films on nickel foil and graphite were 135, and 195 F g−1, respectively[16].

1.7.2.3.5. Tin oxide (SnO_2) based supercapacitors

The long cycle life and stability of the SnOx coatings on graphite was demonstrated in aqueous electrolyte. Wherein alkali metal cations play an important role in the charge–discharge electrochemistry of SnOx coating. A mechanism based on the surface adsorption of electrolyte cations (C+) such as K+ on SnOx could be suggested as follows and simultaneously, the intercalation of H+ or alkali metal cations (C+) in the bulk of the coating upon reduction followed by de-intercalation upon oxidation.

Reasonably high conductivity of SnOx and the formation of nanostructured and microporous material could be attributed to more electrolyte cations adsorbed on the large surface, and preferred the high values of capacitance found in the present study[16].

1.7.2.3.6. Vanadium oxide (V_2O_5) based supercapacitors

Recently, amorphous vanadium oxides (V_2O_5) have received a lot of attention as electrode materials for supercapacitors in aqueous and organic electrolytes. Lee and Goodenough prepared amorphous V_2O_5 by quenching V_2O_5 powders heated at 1183 K and reported its supercapacitive behavior in KCl aqueous electrolyte with Sc of 350 F g−1. They proposed that the K+ ions in the KCl aqueous electrolyte were responsible for the supercapacitive redox reaction of amorphous V_2O_5. V_2O_5 is also known to have electrochemical redox reactions with Li ions in an organic electrolyte as in lithium secondary batteries[16].

1.7.2.3.7. Iron oxide (Fe3O4) based supercapacitor

Recently, iron based materials (Fe_2O_3, Fe_3O_4 and FeOOH) have received attention as promising anode materials due to their variable oxidation states, high theoretical capacitance, natural abundance, low cost and high over-potential for H_2 evolution. Guan

et al. have achieved capacitance of 450 mF/cm2 at the density of 20 mA/cm2 and the electrode was stable for 50000 cycles and retained 111% of its capacitance[17].

1.8. Conclusions

Fig. 5 shows the Sc values obtained for different metal oxide thin film based supercapacitors. Most of the values range between 50 and 1100 F g−1. From the published data, following conclusions can be drawn:

(i) Simple chemical methods such as electrodeposition, spray pyrolysis, chemical deposition, spin coating, dip dry etc. have been employed to deposit metal oxide thin films.

(ii) For most of the systems, only specific capacitance (Sc) values have been reported and the values of interfacial capacitance, specific energy and specific power are not studied.

(iii) In general, stability of electrodes has been reported only for 1000 cycles.

(iv) No asymmetric devices (except MnO2) have been formed.

(v) Amongst the metal oxide materials, only RuO2, MnO2, NiO and Co3O4 thin film based systems have been paid more attention.

Chapter 2. Structural and Electrochemical Characterization Techniques

Structural and electrochemical characterization techniques play crucial roles in the design of nanostructured electrode materials for supercapacitors. These techniques helps researcher to determine what phase of materials was achieved and how it behaves in a particular electrochemical system. Always scanning electron microscope (SEM) is first done one the samples to get a visual idea of how the material is formed, porous, nonporous, well connected structure, etc. To get a better visual understanding of the materials at a much much higer zoom level (10^{-10} m), transmission electron microscope (TEM) is done on the sample. X-ray diffraction (XRD) is an effective instrument to provide samples phase and crystalline structure. Thermogravimetric analysis (TGA) can help to determine the proper ratio of various materials in a composite material. Energy-dispersive X-Ray (EDX) spectroscopy which can be done on the same instrument of SEM gives information about distribution of specific materials in the composite materials. X-Ray photoelectron microscopy is a very necessary characterization technique used to determine oxidation states and elemental composition in the composites. Hence when working on nano-scale materials, these techniques helps to characterize materials for a researcher and then he can modify the experiment to achieve expected results in a proper way. In addition, electrochemical analysis is also indispensable for this project to evaluate the electrochemical performance of the as-synthesized materials. Several electrochemical analysis techniques such as cyclic voltammetry (CV), galvanostatic charge-discharge (GCD), electrochemical impedance spectroscopy (EIS) were done to analyze their behavior in aqueous system[Fan, Xingye].

2.1. Scanning Electron Microscopy

Scanning electron microscopy is an electron microscope which can obtain sample's information by using electron beams to scan the surface of samples and obtain 3D high-resolution images. It is an effective instrument to detect the topology and composition of samples, which allows researchers to unveil the morphology and the structure of microscale and nanoscale materials. A typical SEM image is shown in the following figure

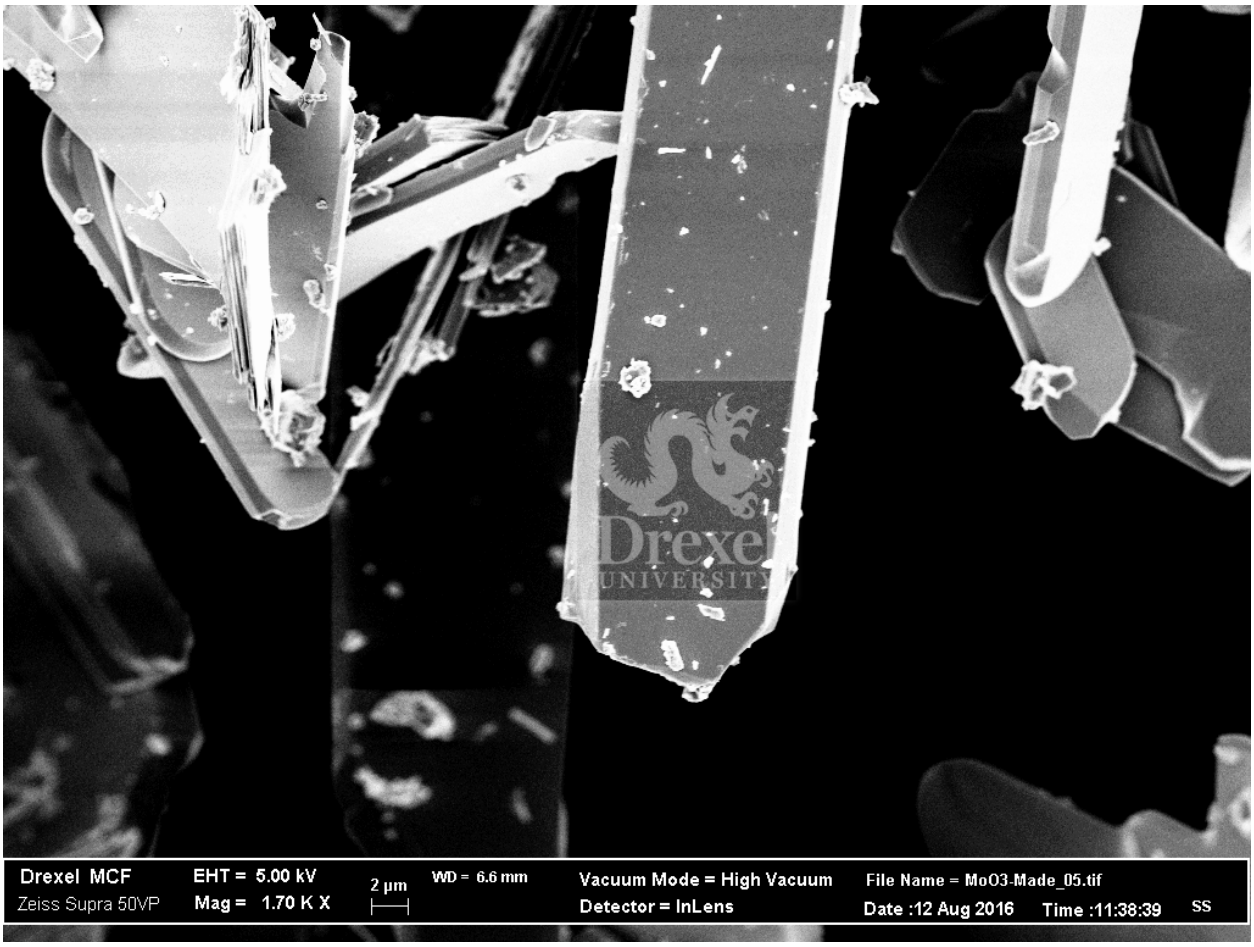

Figure 2.1 SEM image of MoO3 Nanosheets

SEM results in images of with lesser zoom resolution as compared to TEMs, to confirm the presence of micropores and smaller particles embedded, higher resolution images should be used

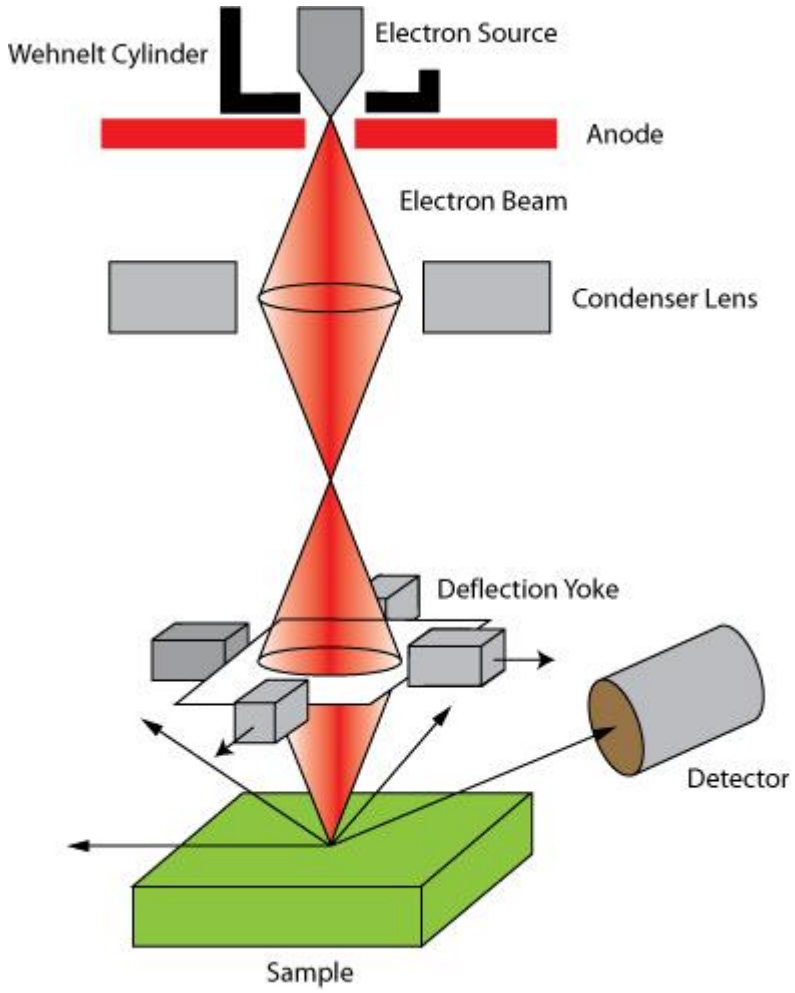

Figure 2.2 Schematic of SEM (JSM-5410, courtesy of JEOL, USA).

The Figure 2.2 has shown the general configuration of a SEM. Basically the SEM has a column shape. On the top of the columns is the electron gun which can produce electrons with the energy of 0.1-30 keV. Below the electron gun is the condenser lens, apertures, and objective lens, which can help to reduce the diameter of electron beam and focus the electron beam on the specimen. To prevent the electrons from being scattered by air, a high-vacuum atmosphere with less than 10-5 mbar is created.

When is SEM is working, electrons are produced by the electron gun and accelerated by electric field to reach a high energy level. Subsequently, the beam is condensed by

condenser lens and apertures to 25 nanoscale and reaches the specimen holder to scan samples. After electrons interact with samples, the properties of samples will be reflected, collected, amplified and produced as high-resolution images.

2.2. Transmission Electron Microscopy

Transmission electron microscopy is another microscopy technique, which is similar to SEM. However, in a TEM, an ultra-thin specimen which is less than 200 nm is used so that a beam of electrons can transmitted through the specimen. The beam of electrons with high energy will interact with the sample and form a high-resolution image. Basically, TEM is able to get images with higher resolution than SEM, because an electron has extremely short de Broglie wavelength which can allow researchers to explore the details such as a single atom and the arrangement of crystal lattices.

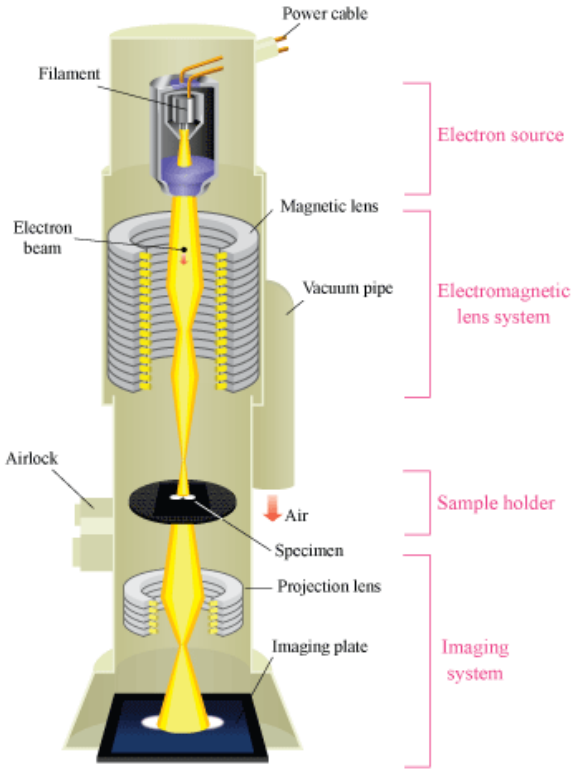

Figure 2.3 A schematic view of a TEM.

The configuration of a TEM is similar to a SEM. A TEM system generally consists of an electron gun, electron lens, apertures, a specimen stage, and a vacuum system. The electron gun is on the top of the whole system and is the electron source. After electrons are emitted from the electron gun, they will be accelerated. Different from SEM, the energy of electrons is 100 keV-400 keV which is much higher than the energy in SEM. As shown in Figure 2.3, apertures and electron lens are below the electron gun which can condense the electron beam. Electron lens is mainly operated by electrostatic or electromagnetic methods to focalize parallel electron rays. Subsequently, the electrons will interact with the sample to form transmitted images which are projected onto the florescent screen.

2.3. Surface area analysis (B.E.T)

Nitrogen adsorption/desorption isotherm technique is a powerful tool to identify the surface area and pore volume of porous materials. The adsorption/desorption is carried out at very low temperature, around the boiling temperature of liquid nitrogen. Generally, the adsorption of gas molecules on solid surface is reversible because of the weak physical bond with Van der Waals force. Dependence on the pore structure of different materials, the adsorption/desorption isotherm (an analysis method) can be classified into various types. Six basic types of Nitrogen adsorption/desorption isotherm are shown in the following figures. Herein, Type I isotherm generally occurs in materials with micropores. Type II isotherm indicates non-porous materials. Type III isotherm shows a typical plot of vapour adsorption. Type IV and V isotherms with hysteresis loop indicates the presence of capillary condensation in mesoporous materials. Type VI isotherm usually occurs in special carbon.

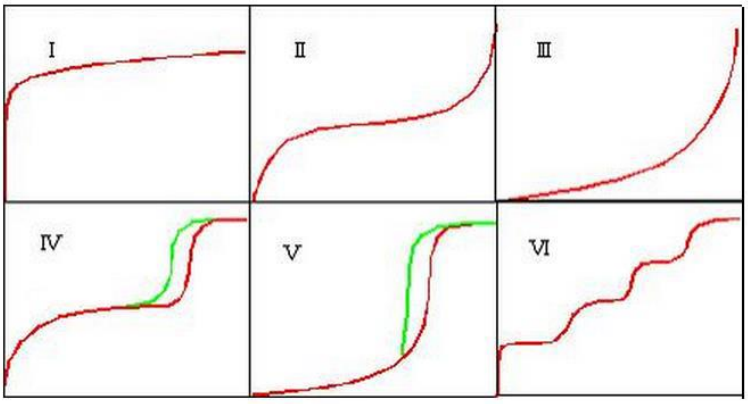

Figure 2.4 Different types of Nitrogen adsorption/ desorption isotherms.

The sample which is going to be tested is kept at liquid nitrogen temperature. Adsorbate is introduced consecutively to the sample. Due to the injection of adsorbate gas, the pressure decreases and becomes stable at the equilibrium pressure. The equilibrium pressure is measured with the increase of the amount of gas that is adsorbed. Finally, the

amount of gas which is adsorbed can be calculated from the equilibrium pressure. Based on the BET theory, which is established and named by Stephen Brunauer, Paul Hugh Emmett, and Edward Teller; the specific surface area can be obtained by Nitrogen adsorption/desorption method. The BET theory is an extension of Langmuir theory upon some proper hypotheses. The principle of BET theory is specifically shown in the following equations:

$$1\ v[(p0\ p\ )\ -\ 1]\ =\ c\ -\ 1\ vmc\ (\ p\ p0)\ +\ 1\ vmc \tag{10}$$

where *v* is the volume of absorbed gas, *p* is equilibrium pressure, *p0* is saturation pressure, *vm* is the volume of monolayer absorbed gas, and *c* is the BET constant. The BET constant can be determined by the following equation:

$$c\ =\ exp\ (E1\ -\ EL\ RT\ ) \tag{11}$$

where *E1* and *EL* are the first layer heat of adsorption and other layers heat of adsorption. Suppose if $\varphi = p/p0$, the Equation can be written as a function of $1v \cdot \varphi\ 1-\varphi$ with φ as the variable. The function can be plotted as a straight line when φ is in the range of $0.05 < \varphi < 0.35$ Suppose if the slope of the straight line is *A* and the y-intercept is *I*, it is possible to obtain the following equations:

$$vm\ =\ 1\ A\ +\ I\ (16)\ c\ =\ 1\ +\ AI \tag{12}$$

Finally, the specific surface area (BET surface area) can be determined by the following equation:

$$SBET\ =\ (vmNs)\ Va \tag{13}$$

Where vm is molar volume of the monolayer adsorbate gas, *N* is the Avogadro's number, *s* is the cross section of the adsorbing species, *V* is the molar volume of absorbate gas, and *a* is the mass of adsorbent.

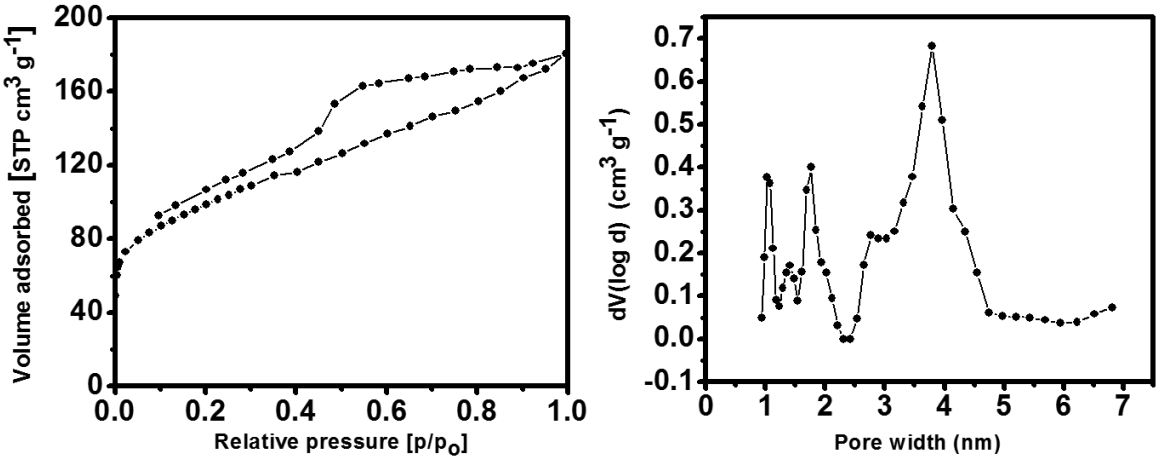

Figure 2.5 Surface area analysis using N2 adsorption isotherm and pore size distribution

2.4. X-ray Photoelectron Spectroscopy

X-ray photoelectron spectroscopy (XPS) technique focuses on the surface chemical characterization from the top 0 to 10 nm of a sample to measure the elemental composition of the surface, empirical formula of pure materials, elements that contaminate a surface, chemical or electronic state of each element, and uniformity of elemental composition. To analyze the bulk of a material, some treatment is necessary such as fracturing, cutting, and scraping to remove the contamination on the surface and expose the deep layer for further characterization.

The samples of XPS are usually solid, since XPS requires high vacuum atmosphere, approximately an ultra-high vacuum, less than 10-9 millibar. When a sample material is

irradiated by the X-ray beam, the electrons on the surface of the material will escape, and it is able to measure the number and kinetic energies of the electrons. Then, the binding energy can be determined by the following equation:

$$Ebinding = Ephoton - Ekinetic - \emptyset \quad (14)$$

Where Ekinetic is the kinetic energy of the escaped electrons, Ephoton is the energy of incident X-ray photon, and ∅ is the work function which depends on both spectrometer and the material. Ephoton is a known energy which can be calculated.

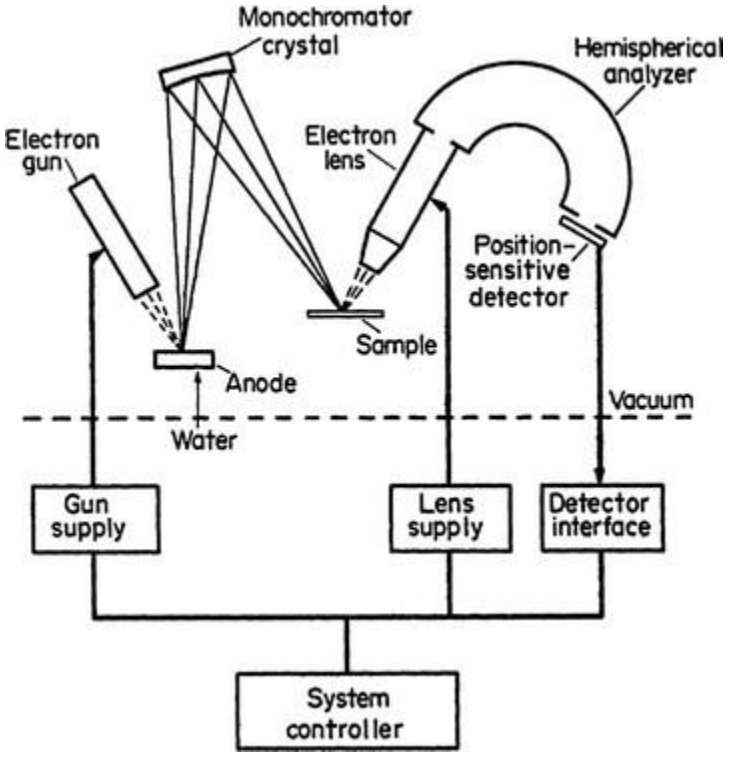

Figure 2.6 A schematic view of the configuration of the XPS.

As shown in Figure 2.6, the emitted electrons, resulting from the irradiation of X-ray, are received by the electron collection lens. The kinetic energy of the emitted electrons will be analyzed by the electron energy analyzer and be converted to XPS signals.

2.5. Conductivity:

The classic arrangement is to have four needle-like electrodes in a linear arrangement with a current injected into the material via the outer two electrodes. The resultant electric potential distribution is measured via the two inner electrodes. By using separate electrodes for the current injection and for the determination of the electric potential, the contact resistance between the metal electrodes and the material will not show up in the measured results. Because the contact resistance can be large and can strongly depend on the condition and materials of the electrodes, it is easier to interpret the data measured by the four-point probe technique than results gathered by two-point probe techniques.

In general, the material's sheet resistivity, r, can be calculated by the relationd by the relation (Vmeasured /Imeasured). The resistivity correction factor ~RCF! takes the size of the test structure, the thickness of the material, the size of the electrodes, and the position of the electrodes with respect to the boundary of the test structure into account. Figure 2.7 illustrates the effect of the position of the electrodes with respect to the boundaries of the test structure. By placing the electrodes at the edge rather than in the middle of the test structure, the measured voltage over the inner electrodes will be two times larger because all current has to take the right-half plane. Valdes calculated the RCF for probes parallel and perpendicular to the boundary of a slab.

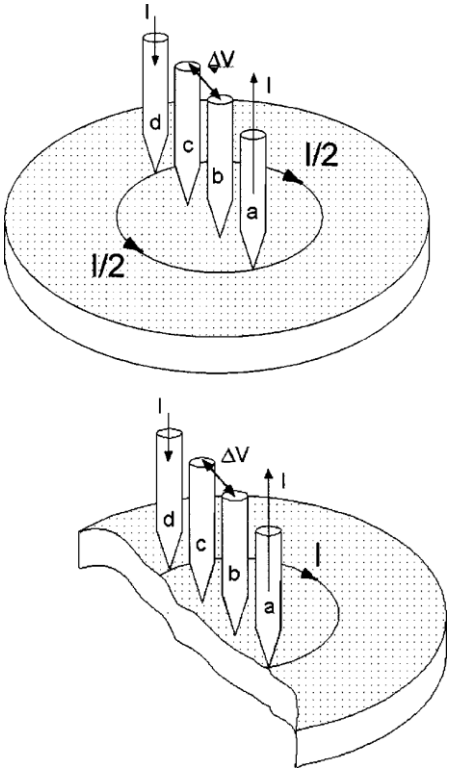

Figure 2.7 Schematic of 4 Probe conductivity measurement

2.6. Supercapacitor Electrochemical Characterization Techniques

Electrochemical characterization techniques are very crucial for the evaluation of the electrochemical performance of electrode materials. Typically, a high-performance supercapacitor electrode material has many necessary properties such as good rate capability, high capacitance, high columbic efficiency, and low electrical resistance. Basic electrochemical characterization techniques involved in supercapacitor evaluation are

galvanostatic charge discharge (GCD), cyclic voltammetry (CV), and electrochemical impedance spectroscopy (EIS).

In order to characterize the electrode material, an active electrode can be tested in a three electrode system, which is common for testing half cells. In a three electrode system, there are three components, working electrode, counter electrode, and reference electrode, where the active electrode is used as the working electrode. To record the potential of this working electrode, a reference electrode whose potential is almost a constant in a narrow potential range is used. In addition, a counter electrode which is usually a platinum wire, is also necessary to carry the current coming across from the working electrode, which can prevent the reference electrode from carrying current, leading to potential change of the reference electrode.

Full cell test, which usually takes place in a two electrode system, can show more practical performance of active materials than half cell, because full cell test works similar to a practical supercapacitor which has a positive electrode and a negative electrode. In a full cell system, both electrodes are assembled with active materials. According to if the active materials in the two electrodes are same or not, the supercapacitor can be divided into symmetric and asymmetric supercapacitor respectively. Depending on Equation (5), the maximum total capacitance is achieved when two electrodes have the same capacitance. Thus, it is significant to control the loading of each electrode to obtain a high total capacitance.

In this project, the working electrode is made from carbon nanofiber mat and it is assembled in a T-Pipe fitting PFA Swagelok setup, the electrode is placed on a 0.5 inch graphite collector and inserted in the setup, the reference electrode is very close to the

working electrode and in this case Ag/AgCl electrode is used as a reference electrode and the counter electrode is a nickel mesh. Figure shows a typical 3 electrode setup.

For a full asymmetric cell setup two dfferent electrodes were used on were used on either of the potential windows and were clubbed together in a 0.5 inch Swagelok pipe fitting as shown in figure. The details of various electrochemical analysis techniques will be discussed in the following sections.

2.6.1. Cyclic Voltammetry

Cyclic voltammetry is a common electrochemical characterization technique to study the electrochemical property of a material. A potential on the working electrode ramps linearly with time from the open circuit potential to a set potential. Then the potential returns to the other set potential in the same way. Both the scan rate and cycles can be controlled. Basically, the redox potential of the active material should be contained within the potential window of CV to analyze the electrochemical property of the material. A typical cyclic voltammogram is shown in Figure 2.8. The corresponding current is a function of the scanning potential. From a cyclic voltammogram, researchers can obtain a large amount of qualitative information with regards to the active material such as the capacitance, conductivity, polarization, reversibility and the position of reduction and oxidation peaks.

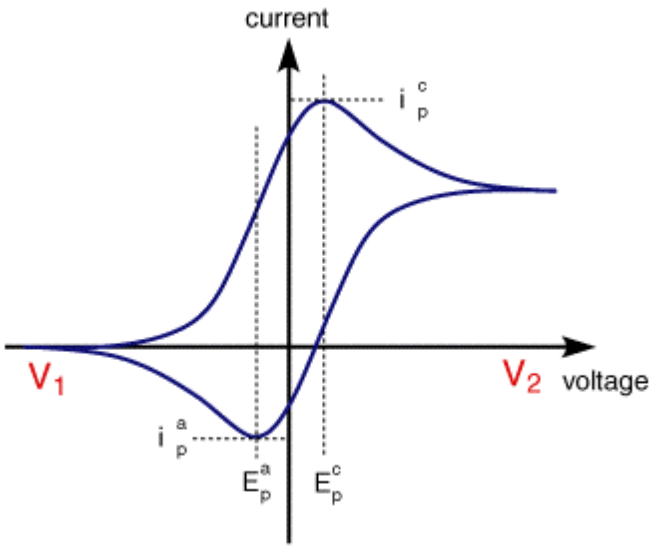

Figure 2.8 a typical cyclic voltammogram

From the area of a CV curve, the specific capacitance of the active material can be calculated with the following equation:

$$C = 1/2\ (\int idv/mvU) \tag{15}$$

where *C* is the specific capacitance, m is the mass of active material, U is the potential window, *v* is the scan rate, and $\int idv$ is the area of the CV curve. Since a cycle contains both charging and discharging processes, the entire area should be divided by two to obtain the specific capacitance. Figure 2.9 Cyclic voltammogram of porous carbonized CNFs in an acidic media tested in a two electrode system.

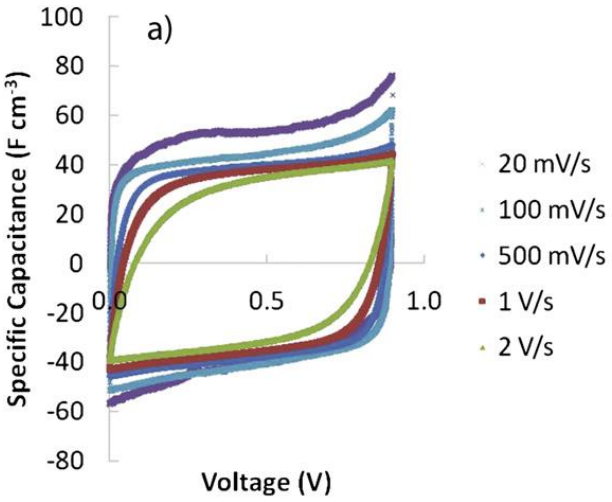

Figure 2.9 CV of CNFs at various scan rates

the CV curve of carbon materials with electric double layer capacitance is similar to rectangular with no redox peaks. With the increase of scan rate, the area of CV curves becomes larger and larger. However, due to the growing resistance at high scan rate, the specific capacitance will slightly decrease. Thus, it is significant to reduce the resistance at high scan rate by developing a rational structure for supercapacitor electrode materials.

2.6.2. Galvanostatic Charge and Discharge

Galvanostatic charge and discharge is a more accurate technique to evaluate the specific capacitance of active materials than CV method. Positive and negative constant currents come across the working electrode to charge and discharge the electrode in a set voltage range with recording the time. A typical GCD curve is shown in Figure 2.10, in which the voltage is drawn as a function of the time. Then, the specific capacitance can be determined by the potential window, current density and discharge time with the following equation:

$$C = I\Delta t\, mU \quad (16)$$

where *I* is the current, Δt is the discharge time, *m* is the mass of electrode material, and *U* is the potential window.

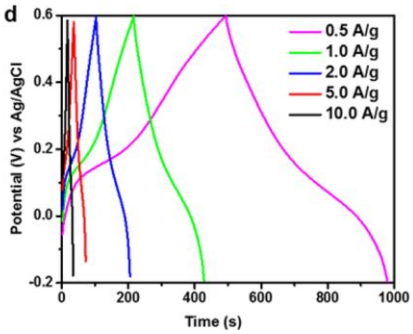

Figure 2.10 Galvanostatic charge-discharge profiles at various current densities of Polyaniline electrode

2.6.3. Electrochemical Impedance Spectroscopy

Electrochemical impedance spectroscopy is a powerful tool to analyze the impedance of an electrochemical system, wherein an alternating potential with changing frequency is applied onto an electrochemical system to test the ratio of alternating potential to the corresponding current signal as a function of sinusoidal wave frequency. The Impedance resulting from the quotient of potential divided by current is a complex number. To use the real part as X axis and the imaginary part as Y axis, it is able to obtain a Nyquist plot, which is important in the analysis of electrochemical impedance. Generally a Nyquist plot consists of a semicircle followed by a 45° straight line. In practice, at high frequency region, the intercept on X axis represents the series resistance of the electrode. The semicircle region mainly reflects charge transfer resistance which is related to reactive

kinetics. At low frequency region, the 45° straight line which is known as Warburg diffusion regime, is attribute to the diffusion transmission resistance in the electrode. However, for some complex EIS curves, the electrochemical system should be studied by representing the system with an equivalent circuit which consists of resistance, capacitance, and inductance etc. basic electrical elements, and analyzed by circuit modelling software.

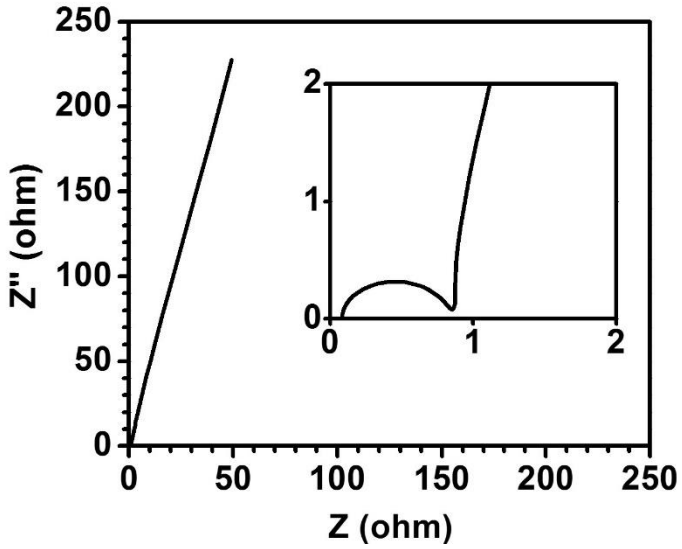

Figure 2.11 Typical plot Electrochemical Impedance Spectroscopy

Chapter 3. Structurally supported Iron Oxide anode

Iron oxides are promising materials for application in supercapacitors owing to their high theoretical redox capacitance (2299 F g^{-1}). Nevertheless, iron oxide nanostructures experience constant stress during cycling due to repeated expansion and contraction resulting in structural degradation. Such structural instability makes it challenging to develop freestanding and binder-free iron oxide based electrodes with superior electrochemical performance. In this work, we report a facile way to fabricate iron oxide based nanofibers using a very simple and fast technique of electrospinning followed by an *insitu* conversion. The final composite electrode consists of iron oxide embedded in carbon nanofibers which possesses a robust contact and support in addition to freestanding and binder-free nature. The electrodes exhibit a capacitance of 460 F g^{-1} at a galvanostatic discharge current density of 1 A g^{-1} and retains ~82% of its capacitance after 5000 cycles in a wide potential window of 1.3 V. Emphasis was kept to monitor ex-situ phase transformation of the electrodes after oxidation and reduction cycles to provide us clear understanding of the redox mechanism taking place during electrochemical cycling.

Keywords: Electrospinning, Iron carbide, Transition metal oxide, Redox mechanism, *in-situ* conversion,Iron oxide, Freestanding, Binder-free.

3.1. Literature review and recent developments

Supercapacitors are amongst the emerging electrochemical energy storage technologies, which possess distinctive merits such as fast charging-discharging rates, exceptionally long cycle life, a wide operational temperature range, superior durability and ease of maintenance[13, 18]. Their aforementioned features have generated great interest for their use in numerous applications viz., back-up power supplies, memory devices, portable electronic devices and hybrid vehicles[11]. However, their limited specific energy, which is a linear function of capacitance and has a square dependence on operating voltage window ($E = ½ CV^2$), is one of the major challenges for their widespread application. In the recent past, there has been a large number of successful attempts in developing asymmetric aqueous supercapacitor devices that widens the operational voltage window by integrating two different electrode materials[19-21]. However, the performance of aqueous asymmetric supercapacitors is so far largely limited by the low capacitance of anode materials[22-23]. There are only a handful of materials — carbon-based (porous carbon, graphene and CNTs) and transition metal oxides (like MoO_3, WO_3 and V_2O_5 with high electron chemical potential) that have been reported as anodes in aqueous supercapacitors[5, 13, 16, 24-25]. For example, Chang and co-workers developed asymmetric supercapacitors (ASCs) using graphene/α-MoO_3 as the negative (anode) electrode, which exhibited a high specific capacitance of ~291 F g^{-1} at 2 mV s^{-1} in 1 M Na_2SO_4 electrolyte with a potential window of -1.0 to 0 V (vs. Ag/AgCl) [5]. Similarly, Qu and co-workers have innovatively grown polypyrrole (PPy) on V_2O_5 using a surfactant to make core shell structured PPy@V_2O_5. High specific capacitance of ~308 F g^{-1} was achieved at a current density of 100 mA g^{-1} in 0.5 mol L^{-1} K_2SO_4 aqueous electrolyte in a window of -0.9 to 0.1 V (vs. SCE)[24]. In another study, Peng and co-workers fabricated WO_3

nanorod bundles and used them as negative electrodes in 1 M H_2SO_4 electrolyte and successfully attained ~385 F g^{-1} at 0.5 A g^{-1} with a anodic voltage window of 0.85 V [25].

Recently, iron based materials (Fe_2O_3, Fe_3O_4 and FeOOH) have received attention as promising anode materials due to their variable oxidation states, high theoretical capacitance, natural abundance, low cost and high over-potential for H_2 evolution[26-27]. However, low electronic conductivity and large volume expansion results in poor rate performance and limited cycling stability[26]. Efforts have been made to improve conductivity by forming composites of these oxides with carbonaceous materials and conducting polymers[27-29]. Even though significant progress has been made using such composites, most of them exhibit short cycle life and poor rate performance[30-32]. This can be attributed to the structural instability/delamination (and subsequent aggregation) of the active material due to the volume expansion during cycling. For example, Wang and co-workers synthesize iron oxide-graphene nanocomposite for supercapacitor application, the electrode exhibited capacitance retention of 86% after 1000 cycles. Wang et al. fabricated single crystalline Fe_2O_3 particles/ graphene composites and the electrode retained 75% of its capacitance after 200 cycles[33]. Limited work has been conducted to address the issue of volume expansion of these oxides for better structural retention and cycle life. Li *et al*. demonstrated a carbon shell protection on Fe_3O_4 nanorods grown on Ti- foil. The anode exhibited a capacity of 275.5 mAh g-1 and retained 64% of its initial capacity after 5000 cycles[34]. However, overall development of anode materials with high capacitance and good cycling stability still remains a challenge.

In this work, we report porous, free-standing, (binder-free) iron oxide anode with significant electrochemical performance in a wide potential window. This anode is fabricated using a simple, fast and a widely scalable electrospinning process. Iron precursor and a polymeric solution is electrospun and the fiber mat is pyrolyzed in an inert environment, resulting in formation of pure iron and iron carbide nanoparticles embedded within the carbon nanofibers. These nanoparticles are converted *in-situ* to iron oxides during the first 35 electrochemical cycles in an aqueous electrolyte system. The interspacing between the nanofibers and robust contact of the iron oxides with conductive carbon nanofiber (CNFs) matrix delivers a good electrolyte / electrode contact, high electronic conductivity along with structural support. CNFs help in cushioning the volume expansion effect of the oxides by withholding the oxide nanoparticles inhibiting rapid structural deformation and improving cycling capabilities. The porous structure further enables good electrolyte penetration inside the fibers which results in reduction in interfacial resistance. The process of using a binder and substrate free technique further eliminates inactive dead weight of the electrode and superiorizes the fiber-electrolyte contact. To better understand the redox reaction mechanism, we have investigated in detail the products formed during the redox reactions via *post mortem* spectroscopic analysis at certain voltages during the charge-discharge process. Fe-CNF electrodes show stable operation in a wide negative potential range (-1.3 to 0 V) vs. Ag/AgCl in 6 M KOH aqueous electrolyte. The synergistic effect present between porous carbon nanofibers (EDLC) and iron oxide (pseudo-capacitive) allowed this composite material to achieve specific capacitance as high as ~460 F g^{-1} at a specific current of 1 A g^{-1} (based

on the mass of the total electrode – carbon and iron compounds). The electrodes retain ~82% of its initial capacitance after 5000 charge-discharge cycles at 1 A g^{-1}.

3.2. Experimental

3.2.1. Materials

Polyacrylonitrile (PAN, M_w = 150,000 g mol^{-1}), Iron acetylacetonate (purity 97%) and N, N-Dimethylformamide (DMF, purity ≥ 99.8%) were purchased from Sigma Aldrich. All chemicals were used without further processing.

3.2.2. Synthesis of Fe-CNFs and physical characterization

The polymer composite solution for electrospinning was prepared by mixing 0.5 g of PAN and 0.5 g of iron acetylacetonate in 4.5 g of DMF solvent. The blend was kept under constant stirring and heating at 60ºC for 10 hours to form a homogenous mixture. Then, the mixture was loaded into a Becton Dickinson 5 mL syringe with a luer lock tip and 18-gauge stainless steel needle (Hamilton Corporation). The syringe with the needle was connected to a NE-400 model syringe pump (New Era Pump Systems, Inc) in order to control feeding rate of the solution. The grounded aluminum collector was placed ~ 6 inches from the tip of the needle. Electrospinning was performed at room temperature with a relative humidity below 15%. A potential difference of 7–8 KV (Series ES (30 KV), Gamma High Voltage Research, Inc) was applied between the collector and the tip of the needle. The flowrate of the solution was kept constant at 0.2 mL $hour^{-1}$. The as-spun nanofibers were collected and stabilized in a convection oven at 280°C for 6 hours in air. Finally, these stabilized nanofiber mats were carbonized at 1000°C for 1 hour with a heating ramp rate of 1°C min^{-1} under a constant flow of nitrogen gas to synthesize iron/iron carbide-carbon nanofibers (Fe-CNFs). These fibers then undergo *in-situ*

conversion of iron/iron carbide to iron oxide during first 35 electrochemical cycles. The complete procedure is schematically shown in Figure 3.1. Carbon nanofibers (CNFs) were also synthesized in the same conditions without using Fe-precursor for comparing the electrochemical performance.

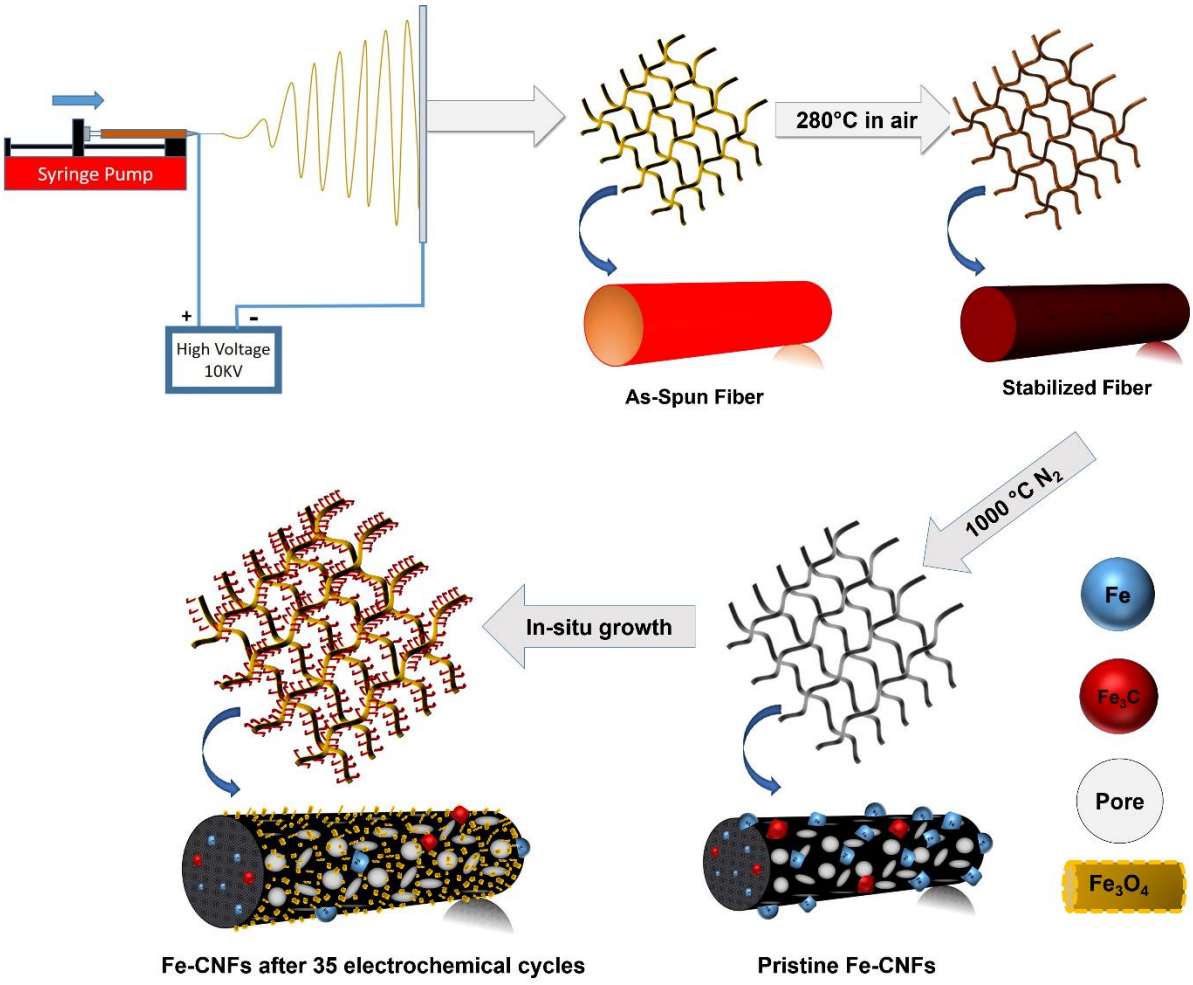

Figure 3.1 Schematic of the fabrication process for the Fe-CNFs

3.3. Physical and Electrochemical Characterizations techniques

Morphological and elemental characterizations of nanofibers were done using scanning electron microscope (Zeiss Supra 50VP) equipped with energy dispersive X-ray spectroscopy (EDS). The average size of the nanofibers was determined using ImageJ software. The phase formation of the Fe-CNFs composite was studied using Rigaku Smart Lab X-ray diffractometer in Bragg–Brentano mode (Cu-K_α as incident radiation with λ=0.1540598 nm) operated at a voltage 40 KV and current 40 mA. The surface chemistry of the sample was analyzed using X - ray photoelectron spectroscopy (Physical Electronics Versa Probe 5000 spectrometer with monochromatic Al K_α as an excitation source). All the XPS spectra were analyzed using CASA XPS software. The surface area of the Fe-CNFs were characterized using nitrogen and CO_2 sorption isotherm. Samples were degassed at -196° C under vacuum for 24 hours to remove the moisture prior to the adsorption-desorption measurements.

All the electrochemical measurements were performed using a three-electrode set up (Swagelok ½ inch T-pipe fitting) with active material (Fe-CNFs) as working electrode, Platinum mesh as the counter electrode and 1 M Ag/AgCl electrode as the reference electrode in 6 M KOH aqueous solution. Working electrode was made by punching free standing as-prepared Fe-CNF mat (thickness 85 microns) with a 13-inch diameter hole punch. Graphite rods were used as current collectors and connected to a potentiostat (Gamry Reference 3000). Cyclic voltammetry (CV) and Galvanostatic charge/ discharge (GCD) tests were conducted at various scan rates (5 mV s^{-1} to 200 mV s^{-1}) and current densities (1 A g^{-1} to 10 A g^{-1}), respectively in a potential window from 0 to -1.3 V (vs. Ag/AgCl). Electrochemical impedance spectroscopy (EIS) measurements were

performed between 5 mHz to 100 kHz frequency range using an AC perturbation of 10 mV rms amplitude.

The specific capacitance (*C)* from the cyclic voltammetry was evaluated using the following equation:

$$C = \frac{\int I dV}{mv} \quad (17)$$

Where i is current response (A), *m* is mass of total electrode (g), and v is scan rate (V s^{-1}). The specific capacitance (*C)* from galvanostatic charge-discharge curves was calculated using the following relation:

$$C = \frac{4I\Delta t}{m\Delta V} \quad (18)$$

Where *I* is the constant discharge current (A), Δ*t* is the discharging time, *m* is the mass of total electrode (g), and Δ*V* is the voltage window (V).

3.3.1. Surface Characterization

The morphological changes in the Fe-CNFs during various thermal treatments were studied using SEM. The as-spun fiber mats were first stabilized in air at 280ºC followed by carbonization at 1000ºC. Fig. 3.2 shows the SEM images of the as-spun, air-stabilized and carbonized nanofiber mats. The as-spun fibers have smooth surface without microscopically identifiable beads and possess diameters ranging from 700 to 900 nm (Fig. 3.2a, b). After the stabilization of the as-spun mats in air, the average diameter of the fibers was reduced to ~600 nm due to dehydrogenation and cyclization of PAN fibers along with simultaneous decomposition of the metal precursor as shown in Fig. 3.2c,d[35].

Finally, in Fig. 3.2e,f, iron nanoparticles with particle size between 5 to 20 nm were observed on the surface of carbonized nanofibers. The average diameter of the carbonized fibers was further reduced to ~400 nm as evident from SEM images. The carbonization of PAN and carbothermal reaction of iron with the carbon matrix resulted in carbon nanofibers with a reduced diameter and embedded iron and carbide nanomaterials[36-38]. The uniform distribution was further confirmed from EDS mapping.

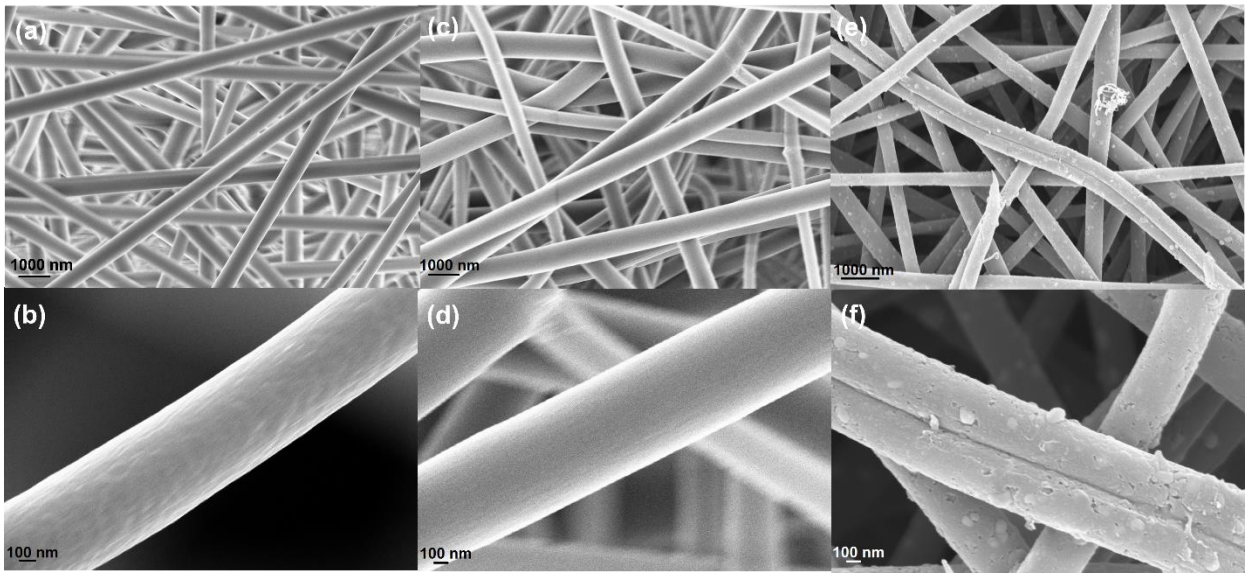

Figure 3.2 Scanning electron microscopy (SEM) images of as-spun nanofibers (a-b) air stabilized nanofibers (c-d) and carbonized nanofibers (e-f).

SEM images show some evidence of porosity in Fe-CNFs. To further determine the porous structure, Nitrogen adsorption/desorption isotherms were measured on Fe-CNFs at 77K on Quadrasorb gas sorption instrument (Quanta-Chrome, USA). The surface area (S_{BET}) and pore volumes (V_t – total pore volume; V_{mic} – micropore volume; V_{meso} – mesopore volume and volume of pores less than 1.0 nm ($V_{<1nm}$)) were determined using

a NLDFT model. Micropore surface area (S_{mic}) and micropore volumes (V_{mic}) were determined from CO_2 adsorption at 0 °C using the Dubinin-Radushkevich (DR) equation (Fig S2).

Table 3.1. BET analysis of the Fe-CNFs samples

	N_2 at -196 °C					CO_2 at 0 °C	
Sample	S_{BET} (m^2/g)	V_t (cm^3/g)	V_{meso} (cm^3/g)	$V_{<1nm}$ (cm^3/g)	V_{mic} (cm^3/g)	S_{mic} (m^2/g)	V_{mic} (cm^3/g)
Fe-CNFs	336.0000	0.2800	0.1750	0.0630	0.1050	122	0.041

N_2 gas sorption was used to quantify the changes in pore structure and accessible surface area after the carbonization of the fiber mat. Fig. 3.3 shows N_2 isotherm and pore size distribution of the fabricated Fe-CNFs. As observed the sample demonstrates multi porous structure with pores <2 nm (microporous) and >2 nm (mesoporous). This may be in the view of the decomposition of metal precursor, polymer and formation of carbides. The surface area analysis as shown in Table 1 of Fe-CNFs showed improvement in porosity and surface area as compared to the CNF samples. Fe-CNFs possess surface area of 336 $m^2\ g^{-1}$ as compared to 29.15 $m^2\ g^{-1}$ of CNFs[10].

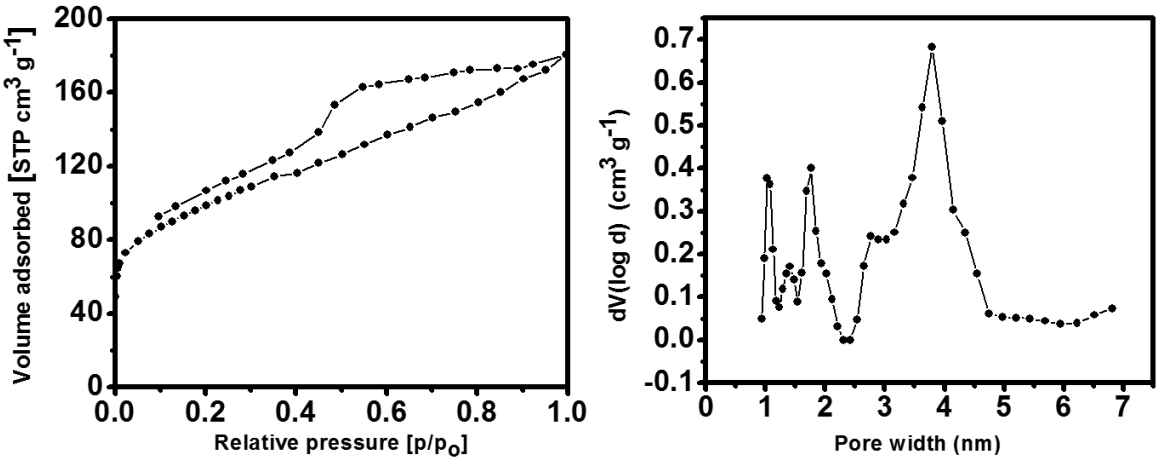

Figure 3.3 (a) N2 isotherm of Fe-CNFs; (b) pore size distribution of Fe-CNFs.

3.3.2. Phase and surface species characterization

The crystallinity and phase purity of the electrode material can have significant effect on the electrochemical performance. Fig. 3.4a shows the XRD pattern of Fe-CNFs. Two diffraction peaks at 2θ = 44.60° and 65.00° were observed, which can be indexed to (110) and (200) planes of α-Fe (JCPDS card 03-065-4899). Other XRD peaks that appeared at 2θ = 37.65°, 37.77°, 42.90°, 43.75°, 45.01° and 51.84° correspond to the planes (112), (021), (121), (210), (103) and (212), respectively for Fe_3C according to JCPDS card 98-000-0170. One broad asymmetric hump between 2θ = 22-28º also appeared indicating the presence of amorphous carbon in nanofibers and some development of graphitic carbon during carbonization of PAN at 1000ºC[39]. The surface composition is of more interest as these species pay a vital role in electrochemical performance. Surface contents of Fe and O species from the pristine Fe-CNFs were determined using high resolution X-ray photoelectron spectroscopy (XPS). As shown in Fig. 3.4b signals of pure iron and iron carbide at 707.09 and 708.2 eV can be seen from the de-convoluted Fe 2p

spectra[40]. Similarly, the O1s spectra (Fig. 3.4c) revealed presence of adsorbed OH^- at 532.6 ev from the surroundings[41-42]. Thus XPS analysis of Fe-CNFs shows presence of iron carbide and iron on its surface. This result further corroborates with the XRD pattern to confirm presence of α-Fe and Fe_3C in the pristine Fe-CNFs.

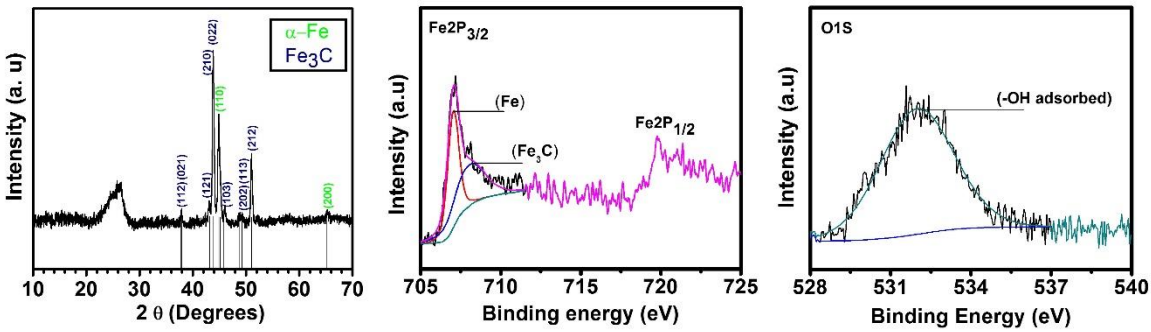

Figure 3.4 (a) X-Ray Diffraction (XRD) pattern and XPS analysis (a) Fe2p and (b) O1s of Fe-CNFs

3.3.3. Electrochemical Characterization

In order to evaluate the electrochemical performance of Fe-CNFs, 3-electrode system was used to perform cyclic voltammetry (CV) and galvanostatic charge-discharge measurements at room temperature in 6 M KOH aqueous electrolyte. We found that the redox peak position/intensities gradually changed in the initial ~10 CV cycles beyond which they stabilized suggesting *in-situ* conversion to a stable redox active iron compound (oxide). In the next section, we elucidate and discuss the fundamental reason for such a change in the initial cycles along with a detailed *post mortem* analysis. In this section, we report the stable electrochemical data obtained after the initial conversion. Fig. 3.6a displays the CV curves of Fe-CNFs tested at different scan rates ranging from 5 to 200 mV s^{-1} in a -1.3 to 0 V versus Ag/AgCl potential window. The quasi-rectangular shape CV curves of the Fe-CNFs stand for a typical pseudocapacitve electrochemical behavior.

Figure 3.5 shows the CV curves of the CNFs (from 10 wt% PAN) and Fe-CNFs at 20 mV

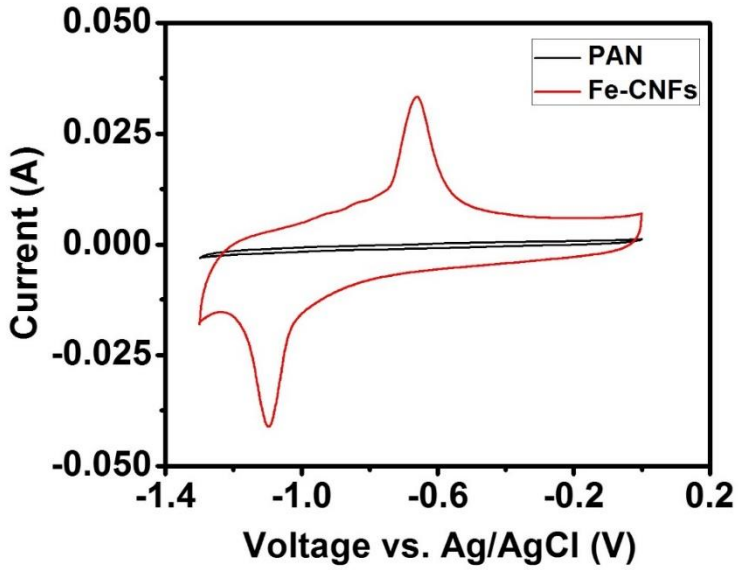

Figure 3.5 CV of Fe-CNF s vs CNF

s^{-1} in a negative potential window. It can be seen that CNFs electrodes exhibited nearly rectangular-shaped CV curves (with no peaks) indicating their electrochemical double layer capacitance (EDLC) type behavior. On the other hand, Fe-CNFs electrodes showed two prominent redox peaks i.e., an oxidation peak at -0.7 V and a reduction peak at -1.1 V vs. Ag/AgCl, implying a strong contribution from the redox reactions along with a better and much wider rectangular shape due to much higher porosity compared to the CNFs. The presence of synergistic effect between conducting porous CNFs (double layer, non-faradaic) and iron oxide (faradaic) possibly contributes to improved redox kinetics and better accessibility of the electrolyte ions. Ultimately, a higher specific capacitance was achieved for Fe-CNFs ~ 325 F g^{-1} in comparison to CNFs ~ 32 F g^{-1} at 20 mV s^{-1}.

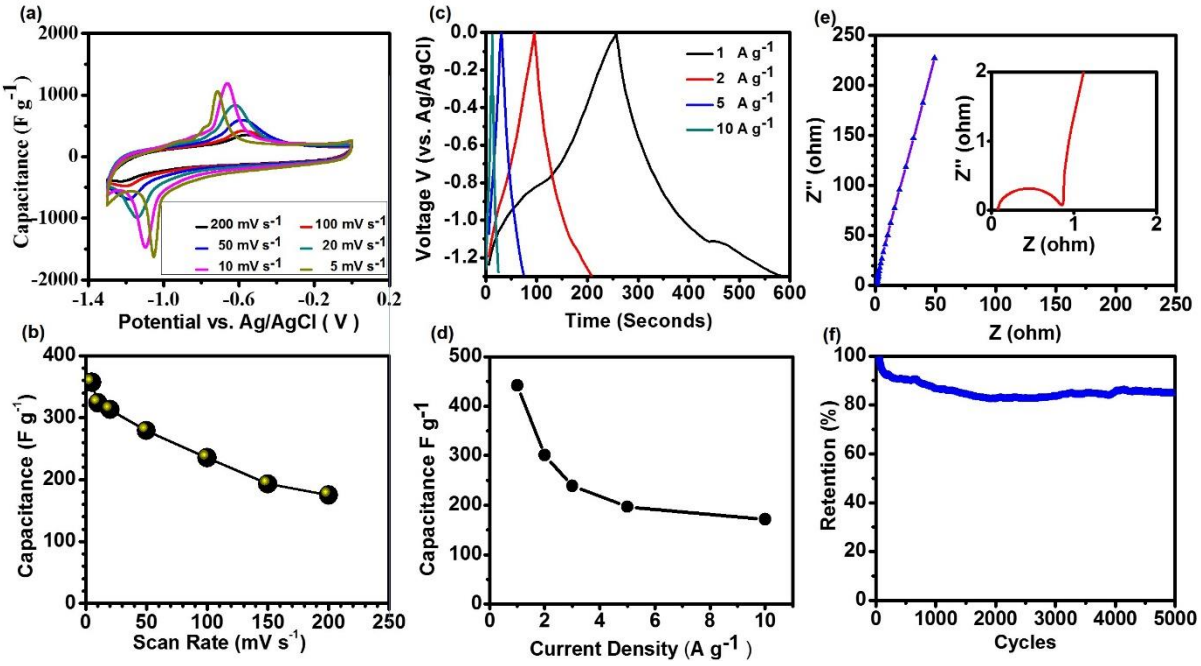

Figure 3.6 (a) CV curves of Fe-CNF's in 6 M KOH electrolyte at different scan rates; (b) Specific capacitance as a function of scan rates; (c) Cyclic charge-discharge curves of Fe-CNFs; (d) Specific capacitance as a function of discharge current densities. (e) Nyq

The symmetric CV curves of Fe-CNFs indicate the reversibility in charge storage and redox reactions. The increase in peak separation with increasing scan rate indicates that the reaction is kinetically limited as the particles are comparatively larger and charge transfer will be restricted at higher scans[43].The specific capacitance values were found to be ~357, 343, 324, 279, 235, 193 and 175 F g^{-1} at scan rates of 5, 10, 20, 50, 100, 150 and 200 mV s^{-1} respectively. The rate capability of Fe-CNFs is shown in Fig. 3.6b which illustrates specific capacitance as a function of scan rate. Further, galvanostatic charge-discharge measurements were carried out (using Equation 2) for Fe-CNFs at various current densities from 1 A g^{-1} to 10 A g^{-1} in a potential window of -1.3 V to 0 V (vs. Ag/AgCl) (Figure 5b). The nonlinear behavior accompanied by plateau regions observed during

charging (at potential -1.1 V) and discharging (at potential -0.7 V) vs. Ag/AgCl are in agreement with the CV results and are further corroborating the presence of faradaic capacitance along with double-layer capacitance. The maximum specific capacitance of ~460 F g^{-1} was observed at 1 A g^{-1}, which expectedly decreased to 171 F g^{-1} at 10 A g^{-1} due to diffusion limitation and underutilization of the active material at higher specific currents (Figure 3.6d). The observed maximum specific capacitance value i.e., 460 F g^{-1} at 1 A g^{-1} is higher than most previously reported Fe-based anode materials in aqueous electrolytes as presented in Table 2. Bulk of the work demonstrates use of binders, wherein the capacitance calculation is based on mass of active material, furthermore the active material may be constituting only a small fraction of iron oxide, rest being some form of carbonaceous material[30, 32, 44-46]. Few of the work focusses, growth of the oxides on substrates, for eg. Li *et al.* have grown iron oxide nano rods on Ti foil / substrate using hydrothermal route and used the substrate as a current collector[34]. Juan *et al.* have grown iron oxide on CNT foam using a novel technique of atomic layer deposition at temperatures which aids decomposition of carbonaceous framework[17]. Fe-CNFs fabricated in this work were binder free and no physical oxidation of carbon fibers were done to make oxides, which makes the fiber morphology brittle, instead we took advantage of electrochemical conversion while cycling to form the active material on Fe-CNFs. Furthermore, Fe-CNFs anodes retained ~82% of the initial specific capacitance when cycled at 1 A g^{-1} over 5000 cycles. This indicates good cyclic stability of the Fe-CNFs composite. This electrode, we believe, exhibits high specific capacitance and rate capability owing to the robust contact of the oxides with the fibers, 3D fibrous architecture, and continuous conductive carbon matrix due to a binder-free format. To further

understand the electrochemical behavior of Fe-CNFs, electrochemical impedance spectroscopy (EIS) measurements were carried out. The typical Nyquist plots observed for Fe-CNFs system exhibited a semicircle located in the high frequency region and a vertical line (close to 90º) in the low frequency region. The diameter of high frequency semicircle (~0.8 Ω) represents charge transfer resistance at the electrode/electrolyte interface. The small charge transfer resistance observed for Fe-CNFs compared to those in the literature could be attributed to good electrical connectivity (due to binder-less preparation), ease of electrolyte accessibility and a large electrode/electrolyte contact region[32, 46-47]. The *x*-axis intercept of the semicircle in high frequency region (~80 mΩ) provides an equivalent series resistance (ESR), which includes contact resistance, electrode material's resistance and bulk electrolyte resistance. The low frequency vertical line indicates nearly ideal capacitive behavior

Table 3.2 A summary of iron oxide composites according to electrolyte, capacitance, retention after cycling and active materials in the electrode used for capacitance calculations.

Composite Materials	Electrolyte	Capacitance F g^{-1} (Current Density)	Retention % (# cycles @ current density)	Active material
Fe_3O_4 NPs[30] §	3 M KOH	185 (1mA)	65 (200 @1 mA)	80
Activated carbon - Fe_3O_4 Nanocomposite [44] §	6 M KOH	120 (5 A g^{-1})	93.66% (1000 @ 1A g^{-1})	85

Porous Fe_3O_4/carbon composite [45] §	1 M KOH	139 (0.5 A g^{-1})	88 (1000 @ 1A g^{-1})	80
Carbon nanotube/ Fe_3O_4 [46] §	6 M KOH	117.2 (10 mA cm^{-2})	91 (500 @ 10 mA cm^{-2})	80
Fe_3O_4/carbon nanofibers [32] §	3 M KOH	225 (A g^{-1})	85 (2000 @ 1A g^{-1})	90
Fe_3O_4 doped porous carbon nanorod [48] §	2 M KOH	285.4 (1 A g^{-1})	104 (5000 @ 2A/g)	
Fe_3O_4 / graphene [49] §	1 M KOH	368 (1 A g^{-1})	~100% (1000 @ 5A g^{-1})	80
Fe_3O_4/reduced graphene oxide [50]	1 M KOH	480 (5 A g^{-1})	115% (1000 @ 10A g^{-1})	100
Fe_3O_4/rGO [47] §	6 M KOH	193 (0.3 A g^{-1})	90.4 (1000 @ 0.5A g^{-1})	80
Fe_3O_4-C [34] #	3 M KOH	247.5 mAh g^{-1} (2mV s^{-1})	64 (5000)	-
GF-CNT- 400 Fe_2O_3 [17] *	2 M KOH	470.5 mF cm-2	111.2(50000 @ 20 mA cm^{-2})	100
Fe-CNFs (This-work)	**6 M KOH**	**430 (1 A g-1)**	**82.5 (5000 @ 1 A g-1)**	**100**

- Active material grown on substrate.

* - Material grown on CNT foam substrate.

§ - composites incorporated with binders.

3.4. In-situ Formation of iron oxides and Elucidation of Redox Mechanism

The alpha Fe and Fe_3C are converted during the initial electrochemical cycles in a potential range of 0 to -1.3 V vs Ag/AgCl. Fe-CNFs when subjected to continuous electrochemical cyclic voltammetry cycles, the intensity of the peaks changes. Fig. 6a shows the first 8 electrochemical cycles where majority of the initial change happens. No peaks are observed in the first reduction cycle. Oxidation peak 1 (Ox1) positioned at - 1V vs. Ag/AgCl shows pronounced peak in the 1st cycle, which reduces on further cycling. This can be attributed to the conversion of Fe to $Fe(OH)_2$ as per the following reaction[8],

$$Fe + 2OH- \rightarrow Fe(OH)_2 + 2e- \quad (19)$$

Intensity of Oxidation peak 2 and Reduction peak 1 gradually increases and become stable after ~10 cycles (Fig. 3.7b). These two stable redox peaks dominant in this anodic region can be assigned to conversion of Fe^{2+} to Fe^{3+} in oxidation and reverse in reduction cycles[51-53]. To understand the changes and the stable active material in redox reactions, *post mortem* XRD, XPS and SEM tests were conducted as various voltage positions during cycling.

3.5. *Post Mortem* XRD and XPS analysis

XRD and XPS analysis were done to identify the phase changes occurring during the stable redox reactions post initial conversion. For sample preparation, electrodes were cycled for 35 electrochemical cycles and held for 1500 seconds at two voltage positions shown in Figure 6b -0.5 V (point 1 after oxidation) and -1.3V (point 2 after reduction).

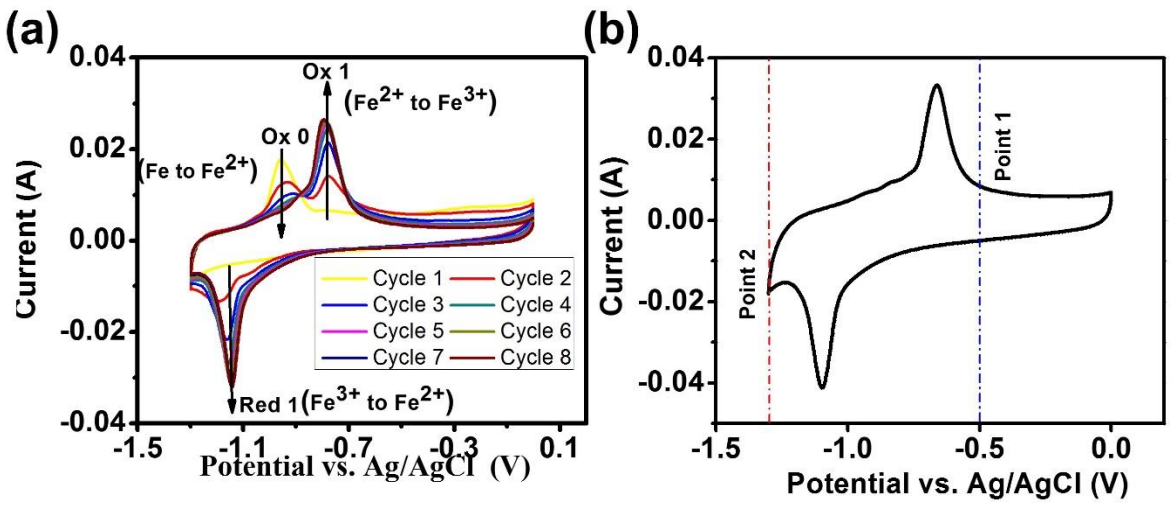

Figure 3.7 (a) First 8 cycles of Fe-CNF's in 6M KOH (b) Fe-CNFs after 35 cycles showing stable redox peaks

The XRD pattern of the sample at point 1 is shown in Fig. 3.8 a. The pattern clearly showed the existence of a new crystalline phase in addition to α-Fe and Fe_3C of the pristine Fe-CNFs sample. The strong peaks at 30.0°, 36.16° and 38.30° could be indexed to (114), (212) and (204) planes, respectively of Fe_3O_4 (JCPDS card 01-075-0449). Moreover, peak intensities corresponding to Fe_3C and Fe were reduced significantly, indicating conversion of those materials to Fe_3O_4. The XRD pattern of the sample held after the reduction cycle at point 2, showed the presence of intense peaks at 2θ = 13.6° and 26.3° in comparison to that of sample at point 1 and pristine samples. These observed peaks can be attributed to (020) and (120) planes of γ -FeOOH (Fe^{3+}), respectively according to the JCPDS card no 08-0098. γ –FeOOH peaks at point 2 suggest the presence of $Fe(OH)_2$ at point 2. Amorphous $Fe(OH)_2$ possibly converted to γ –FeOOH

due to contact with water and oxygen during sample preparation (washing with DI water and drying)[9, 54-57]

$$Fe(OH)_2 + OH^- \rightarrow FeOOH + H_2O + e- \quad (20)$$

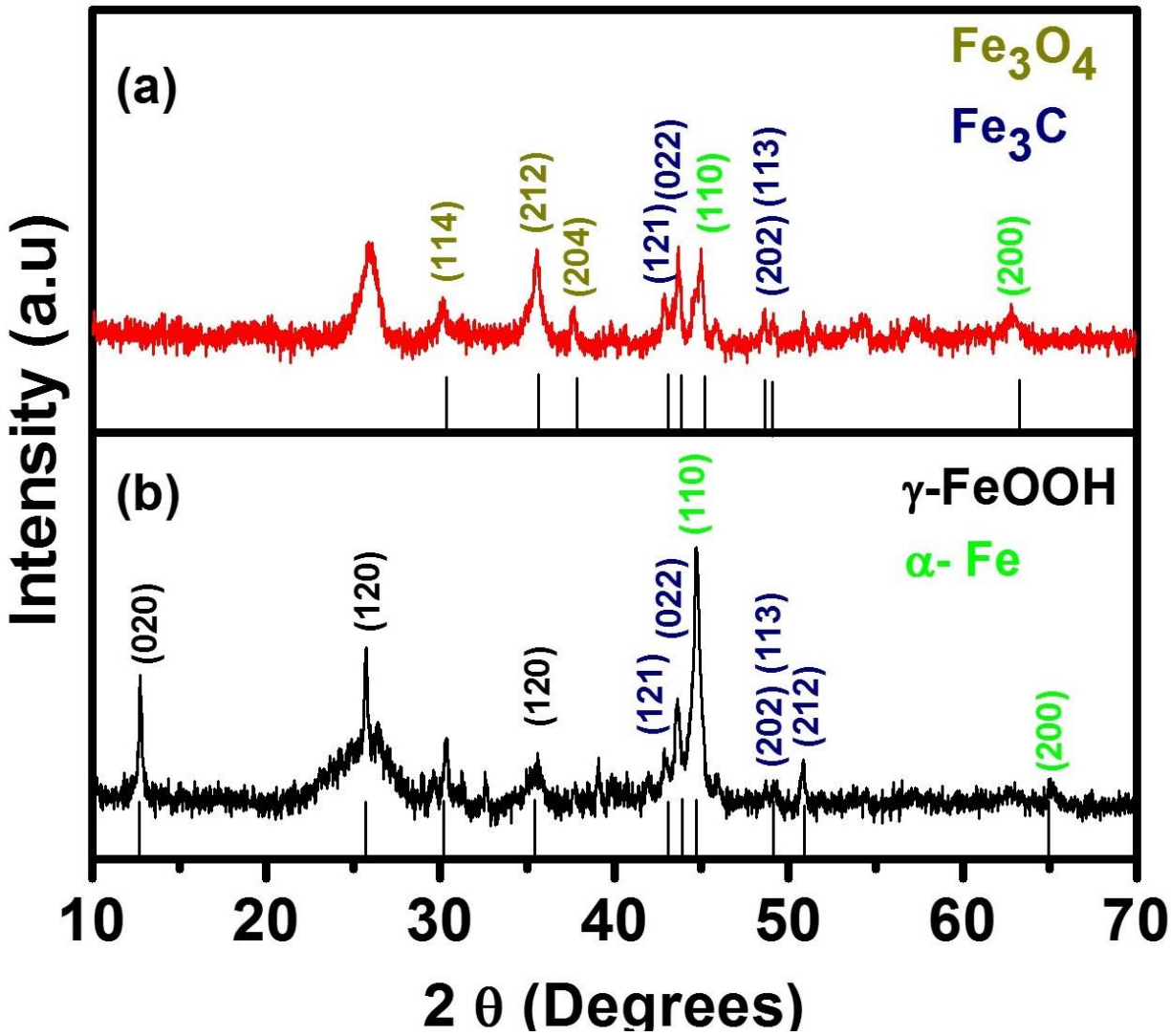

Figure 3.8 XRD patterns of (a) held at -0.5 V (b) held at -1.3 V (vs. Ag/AgCl)

Thus, from the XRD analysis, we believe the stable reaction mechanism to be the conversion of $Fe(OH)_2$ to Fe_3O_4 in the oxidation cycle and the reverse in the reduction cycle. To confirm the product formed after oxidation reaction (i.e., Fe_3O_4) and after reduction reaction (i.e., ϒ-FeOOH) as observed in the XRD, XPS tests were carried out. Peak shifts due to any apparent charging were normalized using the C1s peak set to 284.6 eV.

Figure 8 shows the Fe 2p and O 1s core level spectra for the electrodes held at the two voltage positions – point 1 (-0.5 V) and point 2 (-1.3 V). The Fe 2p spectrum for the sample held at point 1 (Fig. 8 c) exhibited a doublet with $Fe2p_{3/2}$ and $Fe2p_{1/2}$ peaks located at ~711.2 and 724.7 eV, respectively. Further, the $Fe2p_{3/2}$ peak is comprised of four deconvoluted peaks appearing at ~706, 708, 710 and 711 eV, which are associated with α-Fe, Fe_3C, Fe^{2+} and Fe^{3+}, respectively. The presence of Fe^{3+} and Fe^{2+} in this spectrum indicated the presence of mixed oxidation states for Fe. The absence of shakeup peak at 719 eV, which is a significant characteristic of Fe_2O_3, confirmed the presence of Fe_3O_4[58].

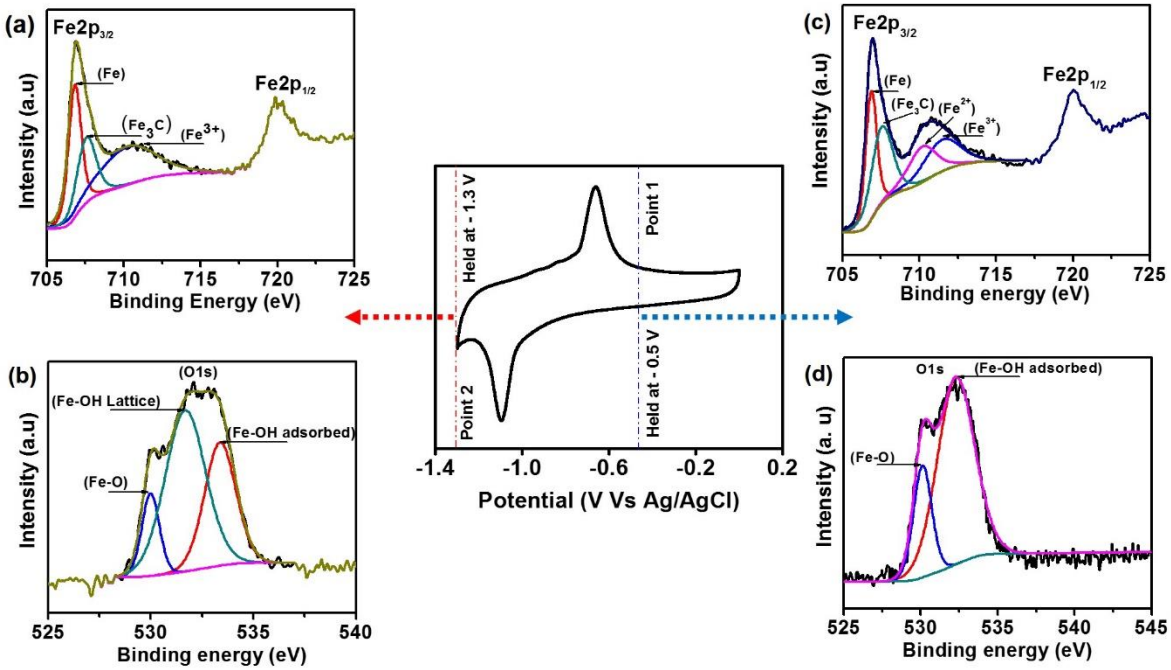

Figure 3.9 Core level Fe 2p and O 1s XPS spectra for the Fe-CNF's held at

The deconvolution of O 1s (Figure 3.9d) spectrum resulted in two strong peaks at 530.4 and 532.6 eV were observed in the O 1s spectra of electrode held at point 1. The peak at 530.4 eV is associated to lattice O^{2-} from Fe_3O_4 (Fe-O-Fe) and the peak at 532.6eV is associated to hydroxyl group (Fe-O-H adsorbed) and water present on the oxide surface due to adsorption[59]. This confirms the presence of iron oxide (Fe_3O_4) at point 1.

Similarly, Fe 2p and O 1s spectrum for the sample held at point 2 (after reduction) were analyzed in order to confirm the presence of Ɣ-FeOOH (as observed in XRD patterns). The de-convoluted peaks at binding energies of ~706, 708 and 711 eV in the Fe 2p spectrum (Fig. 3.9a) show the presence of Fe, Fe_3C and Fe^{3+} species, respectively[42, 60]. Moreover, in O 1s spectrum (Fig. 3.9b), peak at ~530.4 eV is associated with lattice O^{2-} from Fe-O-Fe, peak at ~531.4 eV is associated with lattice hydroxyl group (Fe-O-H lattice), and the third peak at ~532.8 eV is associated with the adsorbed hydroxyl group (Fe-O-H adsorbed) and water present on the surface[41, 57, 59]. These results confirm the

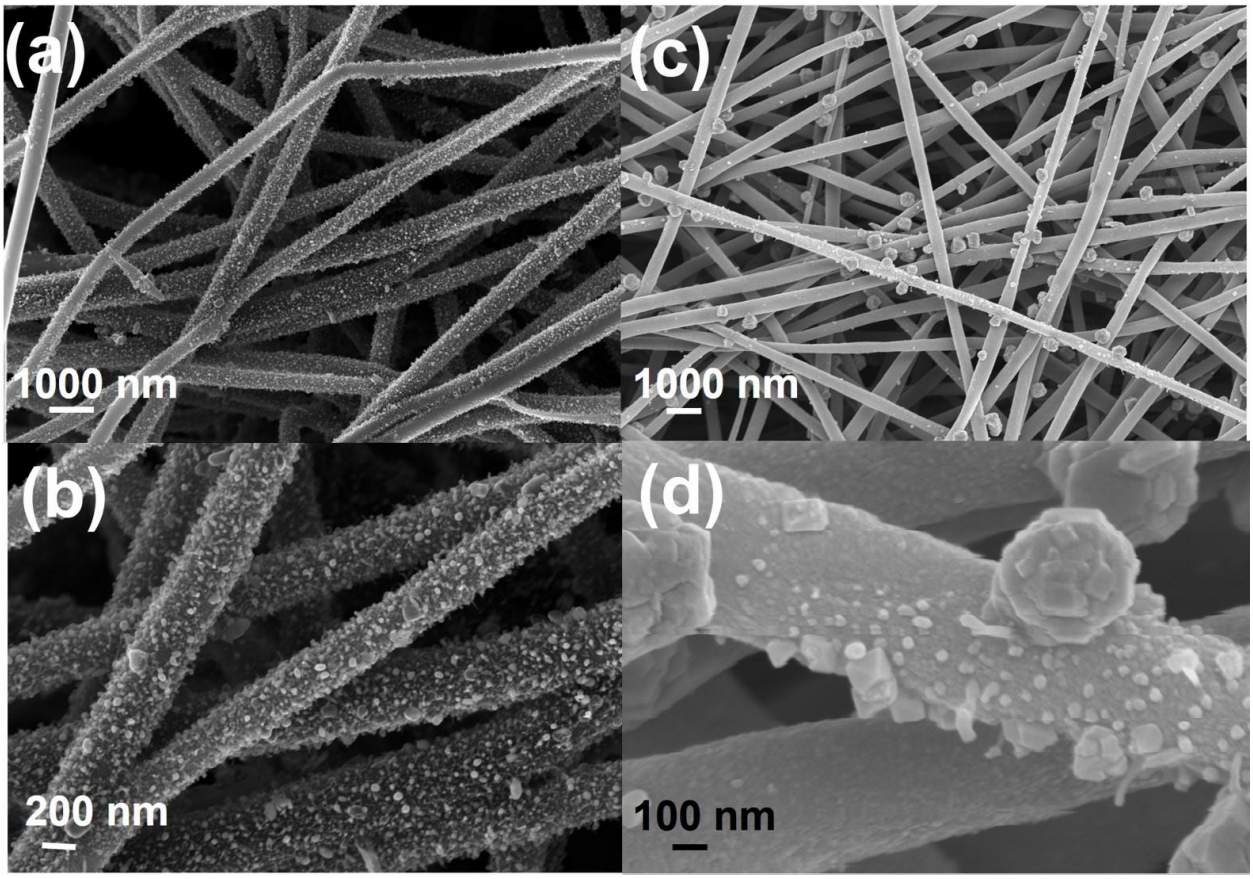

Figure 3.10 (a-b) SEM images of the Fe-CNFs after 35 electrochemical cycles, (c-d) Fe-CNFs after 5000 cycles.

presence of Ɣ-FeOOH resulting from reduction reaction and subsequent conversion from $Fe(OH)_2$.

To summarize, iron and iron carbide formed after the pyrolysis/carbonization is irreversibly converted to $Fe(OH)_2$ and Fe_3O_4 *in-situ* at -1.0 V and -0.5 V (vs. Ag/AgCl) respectively in KOH electrolyte during the initial electrochemical cycles.

Post initial conversion, the CV exhibits well-defined symmetric peaks attributed to the reversible redox conversion of Fe_3O_4 and $Fe(OH)_2$ as per the following reaction,

$$3\,Fe(OH)_2 + 2OH- \leftrightarrow Fe_3O_4 + 4H_2O\ +\ 2e- \quad (21)$$

Fig. 3.10 a, b shows the SEM images of Fe-CNFs after 35 electrochemical cycles and after complete cycling with 5000 cycles. The morphological changes observed on the Fe-CNFs after 35 electrochemical cycles (compared to pristine samples shown in Figure 3.7) can be attributed to the formation of the oxides on the fiber surface as seen from XPS and XRD data. The SEM images of the sample after 5000 cycles shows presence of some embedded material on the fiber surface, Fig 3.10 c, d and XRD pattern (Fig 3.11) confirms the material to be redox Fe_3O_4 (JCPDS - 01-075-0449). The pattern has no peaks associated to iron carbide and α-iron which further confirms complete conversion of the iron carbide and α-iron to redox materials.

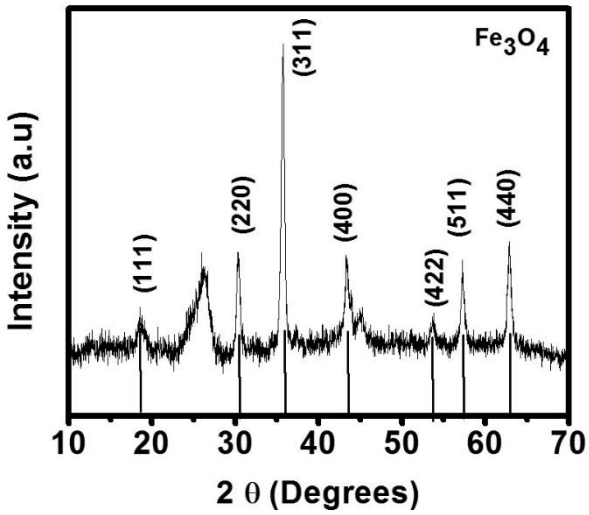

Figure 3.11 XRD pattern of Fe-CNFs after 5000 cycles.

3.6. Conclusion

In summary, we have successfully established a straightforward route to fabricate binder free, porous and free standing Fe-CNFs for supercapacitors via *in-situ* conversion to iron oxide nanoparticles. In addition to its high cycling stability and charge storage capabilities, redox reaction mechanism was elucidated via *post mortem* analysis after oxidation and reduction cycles. The superior stability of the Fe-CNFs for thousands of cycles is attributed to the structural support given by the oxide embedded carbon nanofibers. The good electrochemical response of the oxides form the Fe-CNF's is credited to the interconnected 3-D porous structure and good conductivity provided by the carbon matrix to the oxides. Fe-CNFs renders a large specific capacitance, high performance, low cost and is environmentally safe for energy storage device applications. This fabrication method demonstrated here, can be extended to any other metal oxides, to develop a porous, binder free, free standing electrode for energy storage devices.

Chapter 4. Asymmetric supercapacitor

4.1. Introduction

Supercapacitors / ultracapacitors are devices that bridge the gap between conventional electrostatic capacitors and batteries by combination of redox reactions and EDLC mechanisms and thereby contributing to higher energy density than batteries and capacitors. They are attractive when coupled with batteries and fuel cells for low emission transportation in providing the necessary transient power required for sudden start-up and acceleration, and regenerative recovery of energy from braking. Additionally they can find their applications in back-up power devices in airplanes and other critical power applications like emergency doors on airplanes or other critical places like solar and wind energy sectors. The three main subgroups of supercapacitors are electric double layer capacitors, pseudocapacitors, and hybrid capacitors. As explained earlier, EDLCs store charge electrostatically through surface adsorption of ions from an electrolyte, while pseudocapacitors invoke fast faradaic / redox reactions to chemically store charge in the form of redox products. The dominant electrode material for EDLCs is high surface area carbon, while metal oxides and conducting polymers are the main pseudocapacitive materials. Hybrid supercapacitors, however, are a combination of the two, typically involving a pseudocapacitive and an EDLC electrode. Both metal oxides and conducting polymers have been paired with various carbon electrodes in the formation of hybrid, asymmetric supercapacitor devices.

4.2. Consideration for electrodes:

The idea of a hybrid supercapacitor was put forward because at times a single electrode cannot operate well in both anodic and cathodic region. As stated earlier, the overall energy of the device is dependent on the square of the voltage in which the device operates we need materials which can operate in both anodic as well as cathodic range. Some materials have reported to perform well in the anodic range, while some in cathodic range. This can be further attributed to the fact that the electrode performing in a wider anodic range has high over potential against the hydrogen evolution reaction while the cathode has high over potential against the oxygen evolution reaction. As this being said, a given material cannot possess both the over potential qualities in anodic as well as cathodic zone. Hence materials having higher over potential to hydrogen evolution reaction is coupled with a different material with high over potential to oxygen evolution reaction to make a hybrid asymmetric supercapacitor.

4.3. Device Considerations

4.3.1. Symmetric

As previously described, the energy stored in a supercapacitor, *E*, is defined by its capacitance, *C*, and operational window, *V*, as stated previously. Similarly, total charge storage in the supercapacitor, *Q*, is the derivative of its energy with respect to its operational voltage, leading to Equation:

$$Q=CV$$

The amount of charge each electrode stores must be the same. In symmetric supercapacitors, as both electrodes are made of the same material, they both have the same working potential range, requiring an equalization of the electrodes' capacitance for

charge balancing. As shown previously, Equation 22 shows that, for the two electrodes in series:

$$1/cvtotal = 1/c1 + 1/c2 \quad (22)$$

where *C1* and *C2* correspond to electrode capacitances and *Ctotal* is the total capacitance of the device. Since *C1* = *C2* = *C* for identical electrodes, Equation 8 simplifies the expression to:

$$1/c + 1/c = 2/C\ C = 2Ctotal \quad (23)$$

such that the individual electrodes are twice the total capacitance of the device.

4.3.2. Asymmetric

For asymmetric supercapacitors, this simplification does not hold. Equation 9 shows that the charge storage of both positive and negative electrodes must be the same, such that:

$$CpVp = CnVn = Q \quad (24)$$

where *p* subscripts denote the positive electrode, and *n* subscripts the negative electrode. As the specific capacitance of either electrode in an asymmetric cell is different due to the different electrode material used, Equation 9 can be further broken down as shown in Equation 25:

$$(MCV)p = (MCV)n = Q \quad (25)$$

in which *M* denotes the mass of the respective electrode and C on both sides were decomposed into mass (g) and specific capacitance (F g-1).

The working voltage of a supercapacitor is defined by irreversible reactions, be it the onset of electrolyte solvent decomposition or redox reactions between the electrolyte and electrode.

In the symmetric cell, since electrode masses and specific capacitances are equal, the operational windows of each electrode are also equal. During charging of symmetric cells, each electrode increases in potential and charge at the same rate in opposite directions; because of this, either a positive or negative irreversible reaction acts as limiting factor in the operational window of the cell.

4.3.3. Potential of Zero Voltage (PZV)

In an asymmetric cell, in addition to charge balance other factor which plays an important part is determination of PZV (potential of zero voltage). For example, if positive electrode has oxidation peak at 0.2 V but if the open circuit potential of that electrode is 0.4 V vs Ag/AgCl.The negative electrode has a potential window of 0.5 V but its open circuit potential is 0.3V. When both the electrodes are placed together in an asymmetric system the OCP will show 0 V as its symmetric and the PZV will be 0.35 V vs Ag/AgCl ((0.3 +0.4)/ 2). Both the electrodes will try to maintain electrical neutrality and be both ~0.35V vs Ag/AgCl and 0 V with respect to anode (as anode itself is now at 0.35V vs Ag/AgCl). Now if the charge balance for positive was done based on potential window of 0.7V (0 to 0.7 V) and charge balance of negative electrode was based on potential range of 0.5 (0 to -0.5V) the asymmetric system will perform in 1.2 V window but the positive window would be operating in 0.35 to 1.05V vs Ag/AgCl (vs anode 0.7 V) and negative window would be 0.35 to -0.25 V vs Ag/AgCl assuming the capacitance to be similar in these window as per the calculation, if not this would tend to increase the individual potential more than 1.05 in positive and less than -0.25 in negative or less than 1.05 V in positive and more than -0.5 in negative, further hampering the performance by degradation. More ever we missed the oxidation peak at 0.2 V hence decreasing capacitance of the overall device.

4.4. Asymmetric device electrodes

4.4.1. Anode-Fe_3O_4:

The anode for asymmetric device was Fe-CNFs, whose fabrication is discussed in detail in chapter 3.

4.4.2. Cathode-Co_3O_4:

Recently, Co_3O_4, as a typical pseudocapacitve-type electrode material, has been concerned attribute to its high theoretical capacity, outstanding reversible redox behavior, and good corrosion stability. However, along with other capacitor materials, Co3O4 has suffered with the issues of poor rate capability and cycle stability. In order to improve the energy density of such materials at high rates, it is critical to enhance the ion and electron transfer rate, and thus to ensure plenty electro-active materials occur the Faradic redox reaction. Nowadays, nanostructures (nanowire, nanoflake, nanotube etc.) have been demonstrated to be unique in promoting the mass transport, ion diffusion and electron transport, thus boosting the electrochemical performance. Particularly, this nanostructure directly growth on the substrate usually exhibited much larger capacity than that of nano-powders based materials. In this condition, every nanostructure direct contact with the substrate and thus can make sure that all nanostructures participate in the redox reaction, which increases the utilization of active materials and avoids the “dead zoom” caused by adding ancillary materials (conductive carbon and binder). The open architecture also promote the electrolyte sufficiently contacts. The Co_3O_4 electrode used here is only for demonstration purposes and a lot of work needs to be addressed for optimization.

In this work, we have fabricated cathode, using a simple chemical synthesis approach. First cobalt hydroxide is chemically synthesized and then filtered, the filtered cake is then oxidized at 650 degrees in air for 6 hours for complete conversion to oxides.

4.5. Experimental

4.5.1. Materials

Cobalt acetate and Potassium hydroxide (purity 99%) were purchased from Sigma Aldrich. All chemicals were used without further processing.

4.5.2. Synthesis of Fe-CNFs and physical characterization

2 M solution of cobalt acetate was prepared by mixing 2.77 grams of cobalt acetate in DI water to make 10 ml of solution. To this solution 10 ml of 4 M Potassium Hydroxide (KOH) solution was added slowly with simultaneous stirring at 800 RPM. The final mixture was then stirred at 400 rpm for 3 hours till the mixture completely turned brownish. The mixture was then filtered through Whatman filter paper (Ø = 45 nm) through vacuum filtration setup. The filtered cake was then dried, formed in to a fine powder and then oxidized in a tube furnace under air environment at 650 degree for 6 hours to get Cobalt oxide nanopowder (CNP).

4.6. Physical and Electrochemical Characterizations techniques

Morphological and elemental characterizations of nanofibers were done using scanning electron microscope (Zeiss Supra 50VP) equipped with energy dispersive X-ray spectroscopy (EDS). The phase formation of the CNP was studied using Rigaku Smart Lab X-ray diffractometer in Bragg–Brentano mode (Cu-K_α as incident radiation with λ=0.1540598 nm) operated at a voltage 40 KV and current 40 mA.

All the electrochemical measurements were performed using a three-electrode set up (Swagelok ½ inch T-pipe fitting) with active material (Cobalt oxide slurry) as working electrode, Platinum mesh as the counter electrode and 1 M Ag/AgCl electrode as the reference electrode in 6 M KOH aqueous solution. Working electrode was made by dropcasting cobalt oxide slurry (90% cobalt oxide + 5% conductive carbon + 5% PTFE) on nickel foam. Graphite rods were used as current collectors and connected to a potentiostat (Gamry Reference 3000). Cyclic voltammetry (CV) and Galvanostatic charge/ discharge (GCD) tests were conducted at various scan rates (10 mV s^{-1} to 200 mV s^{-1}) and current densities (1 A g^{-1} to 10 A g^{-1}), respectively in a potential window from 0 to 0.4V (vs. Ag/AgCl). Electrochemical impedance spectroscopy (EIS) measurements were performed between 5 mHz to 100 kHz frequency range using an AC perturbation of 10 mV rms amplitude.

The specific capacitance (*C)* from the cyclic voltammetry was evaluated using the following equation:

$$C = \frac{\int I dV}{mv} \tag{1}$$

Where i is current response (A), *m* is mass of slurry (g), and v is scan rate (V s^{-1}). The specific capacitance (*C)* from galvanostatic charge-discharge curves was calculated using the following relation:

$$C = \frac{4I\Delta t}{m\Delta V} \tag{2}$$

Where *I* is the constant discharge current (A), Δ*t* is the discharging time, *m* is the mass of slurry (g), and Δ*V* is the voltage window (V).

4.6.1. Surface Characterization

The morphological changes in the CNP after oxidation treatment studied using SEM. Fig. 1 shows the SEM image of CNP. The images show formation of symmetrical sized cobalt oxide nanopowder with diameter ranging from 20 to 50 nm (Fig. 4.1).

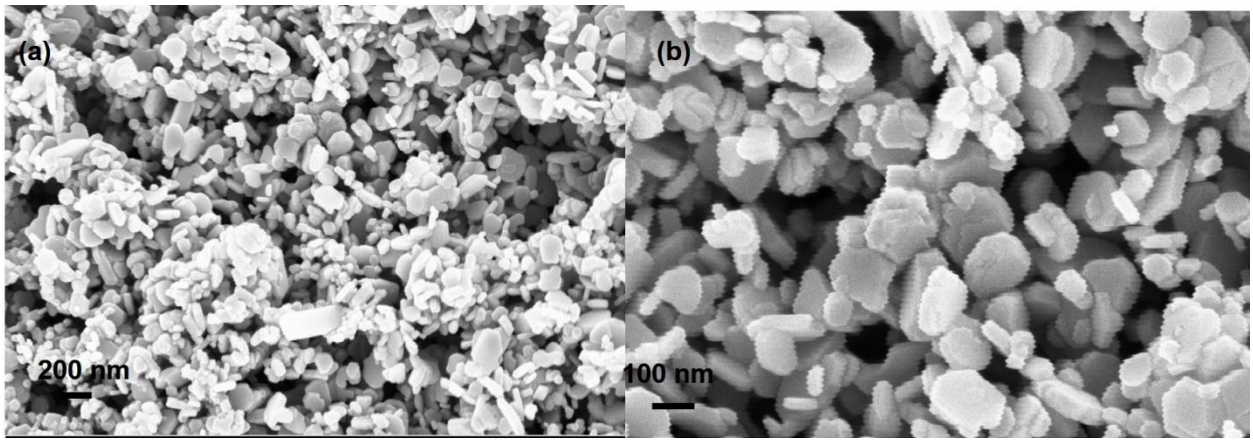

Figure 4.1 Scanning electron microscopy (SEM) images of CNP.

4.6.2. Phase and surface species characterization

The crystallinity and phase purity of the electrode material can have significant effect on the electrochemical performance. Fig. 4.2a shows the XRD pattern of CNP. The diffraction peaks at 2θ = 20.5°, 32°, 37.2°, 45°, 59.6° and 60° were observed, which can be indexed to (111), (220), (311), (400), (511) and (440) planes of Co3O4 (JCPDS card 03-065-4899).

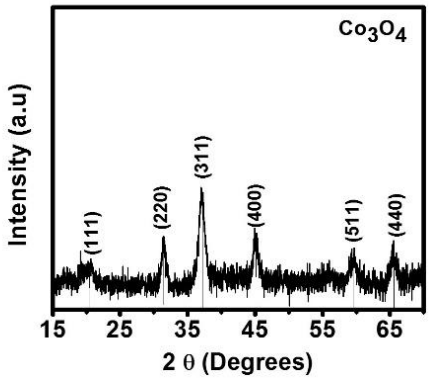

Figure 4.2 (a) X-Ray Diffraction (XRD) pattern of CNP

4.6.3. Electrochemical Characterization

In order to evaluate the electrochemical performance of CNP, 3-electrode system was used to perform cyclic voltammetry (CV) and galvanostatic charge-discharge measurements at room temperature in 6 M KOH aqueous electrolyte. We can clearly see CNP electrodes showed two prominent redox peaks i.e., an oxidation peak at 0.31 V and a reduction peak at 0.29 V vs. Ag/AgCl, implying a strong contribution from the redox reactions but less rectangular shape due to very less porosity.

The symmetric CV curves of CNP indicate the reversibility in charge storage and redox

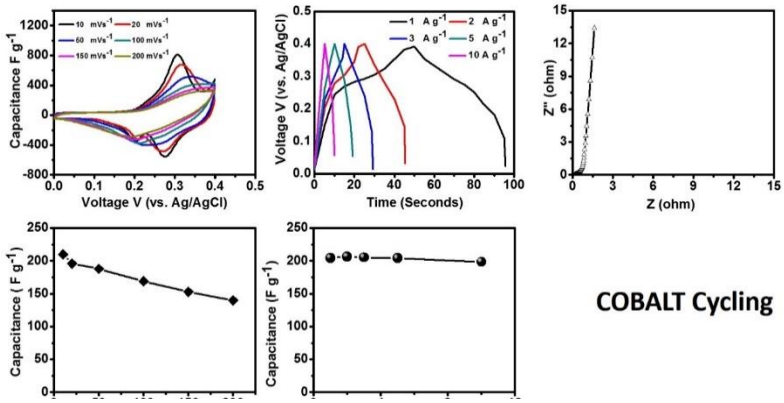

Figure 4.3 (a) CV curves of CNP in 6 M KOH electrolyte at different scan rates; (b) Specific capacitance as a function of scan rates; (c) Cyclic charge-discharge curves of CNP; (d) Specific capacitance as a function of discharge current densities. (e) Nyquist plot

reactions. The increase in peak separation with increasing scan rate indicates that the reaction is kinetically limited as the particles are comparatively larger and charge transfer will be restricted at higher scans[43].The specific capacitance values were found to be ~220, 190,180,175, 160 and 140 F g^{-1} at scan rates of 10, 20, 50, 100, 150 and 200 mV s^{-1} respectively. The rate capability of CNP is shown in Fig. 4.3b which illustrates specific capacitance as a function of scan rate. Further, galvanostatic charge-discharge measurements were carried out (using Equation 2) for CNP at various current densities from 1 A g^{-1} to 10 A g^{-1} in a potential window of 0 to 0.4 V (vs. Ag/AgCl) (Figure 3b). The nonlinear behavior accompanied by plateau regions observed during charging (at potential (0.31 V) and discharging (at potential 0.29 V) vs. Ag/AgCl are in agreement with the CV results and are further corroborating the presence of faradaic reaction. The maximum specific capacitance of ~200 F g^{-1} was observed at 1 A g^{-1}, which exhibited 200 F g^{-1} at 10 A g^{-1} due to good use of the active material at higher specific currents (Figure 2d). Furthermore, CNPs retained ~80% of the initial specific capacitance when cycled at 1 A g^{-1} over 10000 cycles. This indicates good cyclic stability of the CNP composite. To

further understand the electrochemical behavior of CNPs, electrochemical impedance spectroscopy (EIS) measurements were carried out. The typical Nyquist plots observed for Fe-CNFs system exhibited a semicircle located in the high frequency region and a vertical line (close to 90º) in the low frequency region. The diameter of high frequency semicircle (~0.8 Ω) represents charge transfer resistance at the electrode/electrolyte interface. The small charge transfer resistance observed for Fe-CNFs compared to those in the literature could be attributed to good electrical connectivity (due to binder-less preparation), ease of electrolyte accessibility and a large electrode/electrolyte contact region[32, 46-47]. The *x*-axis intercept of the semicircle in high frequency region (~80 mΩ) provides an equivalent series resistance (ESR), which includes contact resistance, electrode material's resistance and bulk electrolyte resistance. The low frequency vertical line indicates nearly ideal capacitive behavior.

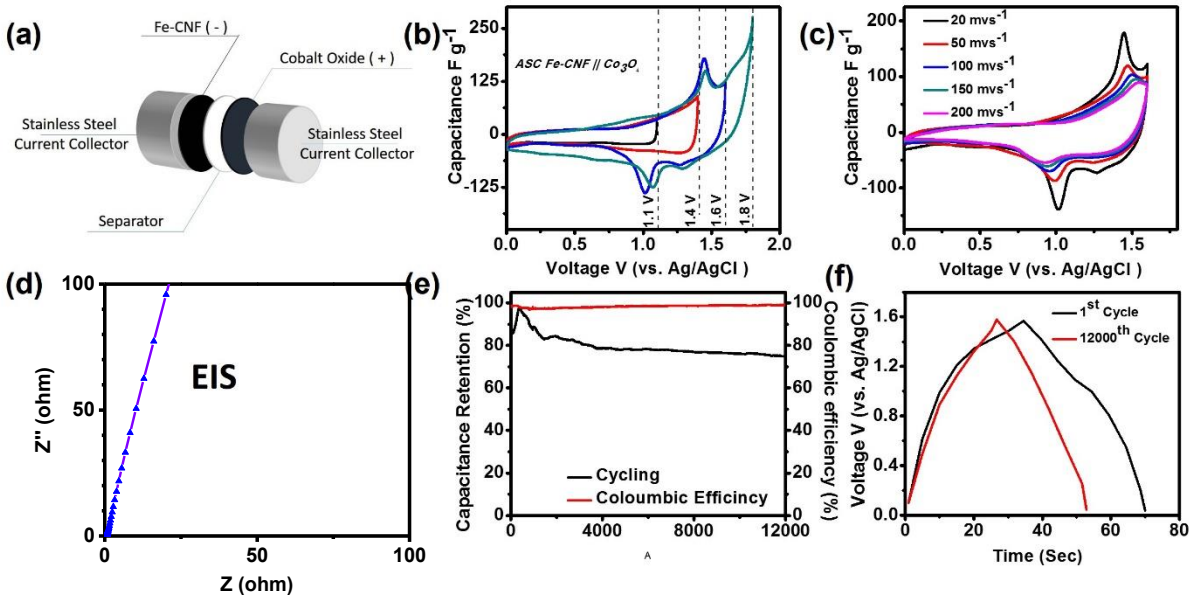

Figure 4.4 (a) CV curves asymmetric Fe-CNFs || Co3O4 supercapacitor, (b) Asymmetric device operated at various voltage ranges; (c) Asymmetric device at various

scan rates; (d) Electrochemical impedance spectroscopy of the whole device; € Coulombic efficiency and cycalbility; (f) Charge discharge curves at 1st and last cycle

4.7. Asymmetric Fe-CNFs|| Co_3O_4 supercapacitor

Herein, we have constructed an asymmetric supercapacitor by employing the Fe-CNFs as negative electrode and Co_3O_4 (CNP) as the positive electrode. The charge ratio of the two electrodes were balanced before making the asymmetric supercapacitor device. The optimal voltage window was determined to be 1.6 V vs Ag/AgCl based on the total performance of the device (Figure 4.4(b)) .As shown (Figure 4.4(c)) cv curves at scan rates for 20 to 200 mV s^{-1} demonstrate that the fabricated asymmetric supercapacitor shows an excellent behavior at 0 - 1.6 V (vs. Ag/AgCl). The capacitance calculated from galvanostatic charge/discharge curves at current density of 1 A g^{-1} shows that specific capacitance of 41 F g^{-1}s was obtained from the device when operated in a range of 1.6 V. The cycling performance of the asymmetric supercapacitor was evaluated at a current density at 1 A g^{-1}. It can be clearly seen that the Fe-CNFs|| Co_3O_4 asymmetric supercapacitor displays excellent cycling stability with about 76% of its initial capacitance even after 12000 cycles (Figure 4.4 e). The positive electrode here is yet to be optimized but it can be inferred that the Fe-CNFs are the potential candidates as anode materials for aqueous supercapacitors.

Reference

1. Wang, K.; Wu, H.; Meng, Y.; Wei, Z., Conducting polymer nanowire arrays for high performance supercapacitors. *Small* **2014,** *10* (1), 14-31.

2. Conway, B. E., *Electrochemical Supercapacitors*. 1999.

3. Singh, A.; Chandra, A., Significant Performance Enhancement in Asymmetric Supercapacitors based on Metal Oxides, Carbon nanotubes and Neutral Aqueous Electrolyte. *Sci Rep* **2015,** *5*, 15551.

4. Wang, Q.; Yu, B.; Li, X.; Xing, L.; Xue, X., Core–shell Co3O4/ZnCo2O4coconut-like hollow spheres with extremely high performance as anode materials for lithium-ion batteries. *J. Mater. Chem. A* **2016,** *4* (2), 425-433.

5. Chang, J.; Jin, M.; Yao, F.; Kim, T. H.; Le, V. T.; Yue, H.; Gunes, F.; Li, B.; Ghosh, A.; Xie, S.; Lee, Y. H., Asymmetric Supercapacitors Based on Graphene/MnO2Nanospheres and Graphene/MoO3Nanosheets with High Energy Density. *Advanced Functional Materials* **2013,** *23* (40), 5074-5083.

6. Simotwo, S. K.; DelRe, C.; Kalra, V., Supercapacitor Electrodes Based on High-Purity Electrospun Polyaniline and Polyaniline-Carbon Nanotube Nanofibers. *ACS Appl Mater Interfaces* **2016,** *8* (33), 21261-9.

7. Wu, Z.; Zhu, Y.; Ji, X., NiCo2O4-based materials for electrochemical supercapacitors. *Journal of Materials Chemistry A* **2014,** *2* (36), 14759.

8. Ravikumar, M. K.; Balasubramanian, T. S.; Shukla, A. K., A nickel-iron battery with roll-compacted iron electrodes. *Journal of Power Sources* **1995,** *56* (2), 209-212.

9. Owusu, K. A.; Qu, L.; Li, J.; Wang, Z.; Zhao, K.; Yang, C.; Hercule, K. M.; Lin, C.; Shi, C.; Wei, Q.; Zhou, L.; Mai, L., Low-crystalline iron oxide hydroxide nanoparticle anode for high-performance supercapacitors. *Nat Commun* **2017,** *8*, 14264.

10. Singhal, R.; Kalra, V., Binder-free hierarchically-porous carbon nanofibers decorated with cobalt nanoparticles as efficient cathodes for lithium–oxygen batteries. *RSC Adv.* **2016,** *6* (105), 103072-103080.

11. Patrice Simon, Y. G., Materials for electrochemical capacitors. *Nature Materials* **2008,** *7*, 845 - 854.

12. Chmiola, J.; Yushin, G.; Gogotsi, Y.; Portet, C.; Simon, P.; Taberna, P. L., Anomalous increase in carbon capacitance at pore sizes less than 1 nanometer. *Science* **2006,** *313* (5794), 1760-3.

13. Zhang, L. L.; Zhao, X. S., Carbon-based materials as supercapacitor electrodes. *Chem Soc Rev* **2009,** *38* (9), 2520-31.

14. Chiang, J.; Macdiarmid, A. G., Polyaniline: Protonic acid doping of the emearaldine form to the metalic regime. *Synthetic Metals* **1986,** *13*, 193-205.

15. Xia, Y.; MacDiarmid, A. G., Camphorsulfonic Acid Fully Doped Polyaniline Emeraldine Salt: In Situ Observation of Electronic and Conformational Changes Induced by Organic Vapors by an Ultraviolet/ Visible/Near-Infrared Spectroscopic Method. *Macromolecules* **1994,** *27*, 7212-7214.

16. Lokhande, C. D.; Dubal, D. P.; Joo, O.-S., Metal oxide thin film based supercapacitors. *Current Applied Physics* **2011,** *11* (3), 255-270.

17. Guan, C.; Liu, J.; Wang, Y.; Mao, L.; Fan, Z.; Shen, Z.; Zhang, H.; Wang, J., Iron oxide-decorated carbon for supercapacitor anodes with ultrahigh energy density and outstanding cycling stability. *ACS Nano* **2015,** *9* (5), 5198-207.

18. Frackowiak, E., Carbon materials for supercapacitor application. *Phys Chem Chem Phys* **2007,** *9* (15), 1774-85.

19. Fan, Z.; Yan, J.; Wei, T.; Zhi, L.; Ning, G.; Li, T.; Wei, F., Asymmetric Supercapacitors Based on Graphene/MnO2 and Activated Carbon Nanofiber Electrodes with High Power and Energy Density. *Advanced Functional Materials* **2011,** *21* (12), 2366-2375.

20. Yan, J.; Fan, Z.; Sun, W.; Ning, G.; Wei, T.; Zhang, Q.; Zhang, R.; Zhi, L.; Wei, F., Advanced Asymmetric Supercapacitors Based on Ni(OH)2/Graphene and Porous Graphene Electrodes with High Energy Density. *Advanced Functional Materials* **2012,** *22* (12), 2632-2641.

21. Lu, X.; Yu, M.; Wang, G.; Zhai, T.; Xie, S.; Ling, Y.; Tong, Y.; Li, Y., H-TiO(2) @MnO(2) //H-TiO(2) @C core-shell nanowires for high performance and flexible asymmetric supercapacitors. *Adv Mater* **2013,** *25* (2), 267-72.

22. Wang, Q.; Wen, Z. H.; Li, J. H., A Hybrid Supercapacitor Fabricated with a Carbon Nanotube Cathode and a TiO2–B Nanowire Anode. *Advanced Functional Materials* **2006,** *16* (16), 2141-2146.

23. Lu, X.; Yu, M.; Zhai, T.; Wang, G.; Xie, S.; Liu, T.; Liang, C.; Tong, Y.; Li, Y., High energy density asymmetric quasi-solid-state supercapacitor based on porous vanadium nitride nanowire anode. *Nano Lett* **2013,** *13* (6), 2628-33.

24. Qu, Q.; Zhu, Y.; Gao, X.; Wu, Y., Core-Shell Structure of Polypyrrole Grown on V2O5 Nanoribbon as High Performance Anode Material for Supercapacitors. *Advanced Energy Materials* **2012,** *2* (8), 950-955.

25. Peng, H.; Ma, G.; Sun, K.; Mu, J.; Luo, M.; Lei, Z., High-performance aqueous asymmetric supercapacitor based on carbon nanofibers network and tungsten trioxide nanorod bundles electrodes. *Electrochimica Acta* **2014,** *147*, 54-61.

26. Zeng, Y.; Yu, M.; Meng, Y.; Fang, P.; Lu, X.; Tong, Y., Iron-Based Supercapacitor Electrodes: Advances and Challenges. *Advanced Energy Materials* **2016,** *6* (24), 1601053.

27. Qu, Q.; Yang, S.; Feng, X., 2D sandwich-like sheets of iron oxide grown on graphene as high energy anode material for supercapacitors. *Adv Mater* **2011,** *23* (46), 5574-80.

28. Lu, X. F.; Chen, X. Y.; Zhou, W.; Tong, Y. X.; Li, G. R., alpha-Fe2O3@PANI Core-Shell Nanowire Arrays as Negative Electrodes for Asymmetric Supercapacitors. *ACS Appl Mater Interfaces* **2015,** *7* (27), 14843-50.

29. Xia, X.; Hao, Q.; Lei, W.; Wang, W.; Sun, D.; Wang, X., Nanostructured ternary composites of graphene/Fe2O3/polyaniline for high-performance supercapacitors. *Journal of Materials Chemistry* **2012,** *22* (33), 16844.

30. Mitchell, E.; Gupta, R. K.; Mensah-Darkwa, K.; Kumar, D.; Ramasamy, K.; Gupta, B. K.; Kahol, P., Facile synthesis and morphogenesis of superparamagnetic iron oxide nanoparticles for high-performance supercapacitor applications. *New Journal of Chemistry* **2014,** *38* (9), 4344.

31. Sun, J.; Zan, P.; Yang, X.; Ye, L.; Zhao, L., Room-temperature synthesis of Fe3O4/Fe-carbon nanocomposites with Fe-carbon double conductive network as supercapacitor. *Electrochimica Acta* **2016,** *215*, 483-491.

32. Fu, C.; Mahadevegowda, A.; Grant, P. S., Fe3O4/carbon nanofibres with necklace architecture for enhanced electrochemical energy storage. *J. Mater. Chem. A* **2015,** *3* (27), 14245-14253.

33. Wang, H.; Xu, Z.; Yi, H.; Wei, H.; Guo, Z.; Wang, X., One-step preparation of single-crystalline Fe2O3 particles/graphene composite hydrogels as high performance anode materials for supercapacitors. *Nano Energy* **2014,** *7*, 86-96.

34. Li, R.; Wang, Y.; Zhou, C.; Wang, C.; Ba, X.; Li, Y.; Huang, X.; Liu, J., Carbon-Stabilized High-Capacity Ferroferric Oxide Nanorod Array for Flexible Solid-State Alkaline Battery-Supercapacitor Hybrid Device with High Environmental Suitability. *Advanced Functional Materials* **2015,** *25* (33), 5384-5394.

35. Fitzer, E.; Frohs, W.; Heine, M., Optimization of stabilization and carbonization treatment of PAN fibres and structural characterization of the resulting carbon fibres. *Carbon* **1986,** *24* (4), 387-395.

36. Schnepp, Z.; Wimbush, S. C.; Antonietti, M.; Giordano, C., Synthesis of Highly Magnetic Iron Carbide Nanoparticles via a Biopolymer Route. *Chemistry of Materials* **2010,** *22* (18), 5340-5344.

37. Wang, X.; Zhang, P.; Gao, J.; Chen, X.; Yang, H., Facile synthesis and magnetic properties of Fe3C/C nanoparticles via a sol–gel process. *Dyes and Pigments* **2015,** *112*, 305-310.

38. Pour, A. N.; Housaindokht, M. R.; Tayyari, S. F.; Zarkesh, J., Fischer-Tropsch synthesis by nano-structured iron catalyst. *Journal of Natural Gas Chemistry* **2010,** *19* (3), 284-292.

39. Sajitha, E. P.; Prasad, V.; Subramanyam, S. V.; Eto, S.; Takai, K.; Enoki, T., Synthesis and characteristics of iron nanoparticles in a carbon matrix along with the catalytic graphitization of amorphous carbon. *Carbon* **2004,** *42* (14), 2815-2820.

40. Bonnet, F.; Ropital, F.; Lecour, P.; Espinat, D.; Huiban, Y.; Gengembre, L.; Berthier, Y.; Marcus, P., Study of the oxide/carbide transition on iron surfaces during catalytic coke formation. *Surface and Interface Analysis* **2002,** *34* (1), 418-422.

41. Grosvenor, A. P.; Kobe, B. A.; McIntyre, N. S., Studies of the oxidation of iron by water vapour using X-ray photoelectron spectroscopy and QUASES™. *Surface Science* **2004,** *572* (2-3), 217-227.

42. Allen, G. C.; Curtis, M. T.; Hooper, A. J.; Tucker, P. M., X-Ray photoelectron spectroscopy of iron–oxygen systems. *J. Chem. Soc., Dalton Trans.* **1974,** (14), 1525-1530.

43. Khani, H.; Wipf, D., Iron oxide nanosheets and pulse-electrodeposited Ni-Co-S nanoflake arrays for high-performance charge storage. *ACS Appl Mater Interfaces* **2017**.

44. Wang, G.; Xu, H.; Lu, L.; Zhao, H., Magnetization-induced double-layer capacitance enhancement in active carbon/Fe3O4 nanocomposites. *Journal of Energy Chemistry* **2014,** *23* (6), 809-815.

45. Meng, W.; Chen, W.; Zhao, L.; Huang, Y.; Zhu, M.; Huang, Y.; Fu, Y.; Geng, F.; Yu, J.; Chen, X.; Zhi, C., Porous Fe3O4/carbon composite electrode material prepared

from metal-organic framework template and effect of temperature on its capacitance. *Nano Energy* **2014,** *8*, 133-140.

46. Guan, D.; Gao, Z.; Yang, W.; Wang, J.; Yuan, Y.; Wang, B.; Zhang, M.; Liu, L., Hydrothermal synthesis of carbon nanotube/cubic Fe3O4 nanocomposite for enhanced performance supercapacitor electrode material. *Materials Science and Engineering: B* **2013,** *178* (10), 736-743.

47. Yan, F.; Ding, J.; Liu, Y.; Wang, Z.; Cai, Q.; Zhang, J., Fabrication of magnetic irregular hexagonal-Fe3O4 sheets/reduced graphene oxide composite for supercapacitors. *Synthetic Metals* **2015,** *209*, 473-479.

48. Wang, L.; Yu, J.; Dong, X.; Li, X.; Xie, Y.; Chen, S.; Li, P.; Hou, H.; Song, Y., Three-Dimensional Macroporous Carbon/Fe3O4-Doped Porous Carbon Nanorods for High-Performance Supercapacitor. *ACS Sustainable Chemistry & Engineering* **2016,** *4* (3), 1531-1537.

49. Liu, M.; Sun, J., In situ growth of monodisperse Fe3O4nanoparticles on graphene as flexible paper for supercapacitor. *Journal of Materials Chemistry A* **2014,** *2* (30), 12068.

50. Shi, W.; Zhu, J.; Sim, D. H.; Tay, Y. Y.; Lu, Z.; Zhang, X.; Sharma, Y.; Srinivasan, M.; Zhang, H.; Hng, H. H.; Yan, Q., Achieving high specific charge capacitances in Fe3O4/reduced graphene oxide nanocomposites. *Journal of Materials Chemistry* **2011,** *21* (10), 3422.

51. Wang, H.; Liang, Y.; Gong, M.; Li, Y.; Chang, W.; Mefford, T.; Zhou, J.; Wang, J.; Regier, T.; Wei, F.; Dai, H., An ultrafast nickel-iron battery from strongly coupled inorganic nanoparticle/nanocarbon hybrid materials. *Nat Commun* **2012,** *3*, 917.

52. Long, C.; Wei, T.; Yan, J.; Jiang, L.; Fan, Z., Supercapacitors based on graphene-supported iron nanosheets as negative electrode materials. *ACS Nano* **2013,** *7* (12), 11325-32.

53. Periasamy, P.; Babu, B. R.; Iyer, S. V., Electrochemical behaviour of Teflon-bonded iron oxide electrodes in alkaline solutions. *Journal of Power Sources* **1996,** *63* (1), 79-85.

54. Whitehead, P. G.; Hall, G.; Neal, C.; Prior, H., Chemical behaviour of the Wheal Jane bioremediation system. *Sci Total Environ* **2005,** *338* (1-2), 41-51.

55. Begum, S. N.; Basha, C. A.; Muralidharan, V. S., Role of Halides on the Passivation of Iron in Alkaline Buffer Solutions. *Portugaliae Electrochimica Acta* **2010,** *28* (3), 143-151.

56. Sudakar, C.; Subbanna, G. N.; Kutty, T. R. N., Effect of anions on the phase stability of γ-FeOOH nanoparticles and the magnetic properties of gamma-ferric oxide derived from lepidocrocite. *Journal of Physics and Chemistry of Solids* **2003,** *64* (12), 2337-2349.

57. Jia, Y.; Luo, T.; Yu, X.-Y.; Sun, B.; Liu, J.-H.; Huang, X.-J., Synthesis of monodispersed α-FeOOH nanorods with a high content of surface hydroxyl groups and enhanced ion-exchange properties towards As(v). *RSC Advances* **2013,** *3* (36), 15805.

58. McIntyre, N. S.; Zetaruk, D. G., X-ray photoelectron spectroscopic studies of iron oxides. *Analytical Chemistry* **1977,** *49* (11), 1521-1529.

59. Baltrusaitis, J.; Cwiertny, D. M.; Grassian, V. H., Adsorption of sulfur dioxide on hematite and goethite particle surfaces. *Phys Chem Chem Phys* **2007,** *9* (41), 5542-54.

60. Antunes, E. F.; de Resende, V. G.; Mengui, U. A.; Cunha, J. B. M.; Corat, E. J.; Massi, M., Analyses of residual iron in carbon nanotubes produced by camphor/ferrocene pyrolysis and purified by high temperature annealing. *Applied Surface Science* **2011,** *257* (18), 8038-8043.